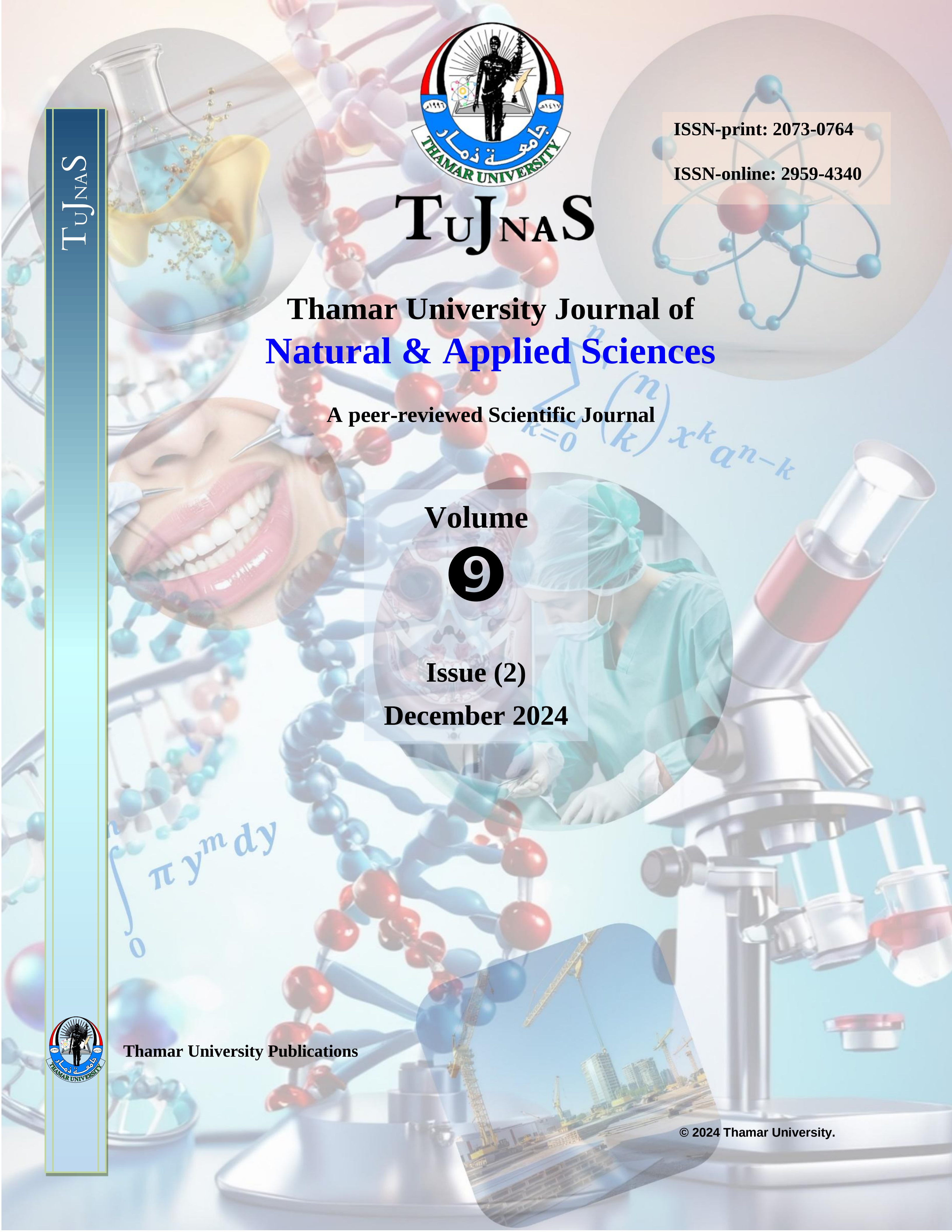

ISSN-print: 2073-0764

ISSN-online: 2959-4340

TUJNAS

Thamar University Journal of Natural & Applied Sciences

A peer-reviewed Scientific Journal

Volume

❾

Issue (2)

December 2024

Thamar University Publications

Thamar University Journal of Natural and Applied Sciences (*TUJNAS*)

Thamar University Journal of Natural & Applied Sciences (TUJNAS) is a peer-reviewed journal. It is an open-access journal published by Thamar University, Dhamar, Yemen twice a year. The aim of the journal is to publish original and review articles in the fields of science, agriculture, engineering, medicine, environment, and computer science. The journal is published in English only.

The journal has the following international standard codes:

ISSN-print: 2073-0764

ISSN-online: 2959-4340

For more information on editorial policy, manuscript submission, ethics, etc., please visit the TUJNAS Journal website:

https://www.tu.edu.ye/journals/index.php/TUJNAS

Editorial Team

General Supervisor

Prof. Dr. Mohammed Mohammed Al-Haifi

Position: Rector of the University, Thamar University, Dhamar, Yemen.

Address: University Presidency, Thamar University, P O Box 87246 Dhamar, Yemen.

E-Mail: dralhaifi@tu.edu.ye

Editor-in-chief

Prof. Dr. Adulkarem Esmail Zabiba

Position: Vice-Rector of Postgraduate and Scientific Research, Thamar University, Dhamar, Yemen.

Address: Vice Presidency of the University for Postgraduate Studies and Scientific Research, Thamar University, P O Box 87246 Dhamar, Yemen.

E-Mail: karimzabiba@tu.edu.ye

Editorial Director

Prof. Dr. Abdullah Ahmed Ali Ahmed

Position: Professor of Nanoscience, Physics Department, Faculty of Applied Sciences, Thamar University, Dhamar, Yemen.

Address: Faculty of Applied Sciences, Thamar University, P O Box 87246 Dhamar, Yemen.

E-Mail: abdullah2803@tu.edu.ye

✉ All correspondence should be sent to: ✉

Editorial Director,

Thamar University Journal of

Natural and Applied Sciences (TUJNAS)

Thamar University, P O Box: 87246 Dhamar, Republic of Yemen
E-Mail: tujnas@tu.edu.ye

Advisory Board

Prof. Dr. Abdulkafi A. S. Al-Refaei

Position: Vice-Rector of Students' Affairs, Thamar University, Dhamar, Yemen.

Address: Vice Presidency of the University for Student Affairs, Thamar University, Dhamar, Yemen.

E-Mail: alrefaei@tu.edu.ye

Assoc. Prof. Adel Abdulgani Lutf Al-Ansi

Position: Vice-Rector of Academic Affairs, Thamar University, Dhamar, Yemen.

Address: Vice Presidency of the University for Academic Affairs, Thamar University, Dhamar, Yemen.

E-Mail: adel.ansi@tu.edu.ye

Prof. Dr. Daiekh Abed-Ali Abod

Position: Professor of Organic and Biochemistry, Department of Biochemistry, Faculty of Medicine, Thamar University, Dhamar, Yemen.

Address: Department of Biochemistry, Faculty of Medicine, Thamar University, Dhamar, Yemen.

E-Mail: prof.dr.daiekh@tu.edu.ye

Prof. Dr. Basheer M. Al-Maqaleh

Position: Dean of Faculty of Computer Sciences and Information Systems, Thamar University, Dhamar, Yemen.

Address: Faculty of Computer Sciences and Information Systems, Thamar University, Dhamar, Yemen.

E-Mail: basheer.almaqaleh@tu.edu.ye

Assoc. Prof. Abdul-Qawe Kaed Dabouan

Position: Dean of Faculty of Applied Sciences, Thamar University, Dhamar, Yemen.

Address: Faculty of Applied Sciences, Thamar University, Dhamar, Yemen.

E-Mail: abdulqawe.dabouan@tu.edu.ye

Copyright © 2024 Thamar University

Assoc. Prof. Abdul Ghani Ali Mohammed

Position: Dean of Faculty of Agriculture & Veterinary Medicine, Thamar University, Dhamar, Yemen.

Address: Faculty of Agriculture & Veterinary Medicine, Thamar University, Dhamar, Yemen.

E-Mail: abdulghani.ali@tu.edu.ye

Assist. Prof. Fouad Mohammed Y. Al-Jarmouzi

Position: Dean of Faculty of Engineering, Thamar University, Dhamar, Yemen.

Address: Faculty of Engineering, Thamar University, Dhamar, Yemen.

E-Mail: aljarmouzi@tu.edu.ye

Assist. Prof. Nashwan Hamid Saleh Al-Tairi

Position: Dean of Faculty of Dentistry, Thamar University, Dhamar, Yemen.

Address: Faculty of Dentistry, Thamar University, Dhamar, Yemen.

E-Mail: nashwanh9@tu.edu.ye

Assoc. Prof. Adel Ali Ahmed Amran

Position: Dean of Faculty of Medical Science, Thamar University, Dhamar, Yemen.

Address: Faculty of Medical Science, Thamar University, Dhamar, Yemen.

E-Mail: adelamran@tu.edu.ye

Assist. Dr. Abdullah Al-Murtadha

Position: Dean of Faculty of Medicine, Thamar University, Dhamar, Yemen.

Address: Faculty of Medicine, Thamar University, Dhamar, Yemen.

E-Mail: abdullah.almurtadha@tu.edu.ye

Editorial Board

Prof. Dr. Samer Hasan Hussein-Al-Ali (Jordan)

Research field: Drug delivery, Chemistry, Controlled Release, Cancer Cells, and Nanomaterials.

Position: Dean of Scientific Research, Faculty of Pharmacy, Isra University, Amman, Jordan

Affiliation: Faculty of Pharmacy & Department of Chemistry, Faculty of Science, Isra University, Amman 11622, Jordan.

E-Mail: samer.alali@iu.edu.jo ,
sameralali72@yahoo.com

Prof. Dr. Khalil Saeed Al-Wagih (Yemen)

Research field: Computer Sciences, Machine Learning, Big Data, Artificial Intelligence, and IoT.

Position: President of Al-Razi University, Al-Razi University, Sana'a, Yemen.

Affiliation: Department of Computer Science, Faculty of Computer Science & Information System, Thamar University, Dhamar, Yemen.

E-Mail: khalilwagih@tu.edu.ye ,
khalilwagih@gmail.com

Prof. Dr. Salem Aqeel (Canada)

Research field: Polymer Nanocomposite, Superhydrophobic, Piezoelectric Polymers, and Lubricating Oils.

Position: Polymer Scientist at GL CHEMTEC INTERNATIONAL LTD., 1456 Wallace Road, Oakville Ontario, Canada.

Affiliation: GL CHEMTEC INTERNATIONAL LTD., 1456 Wallace Road, Oakville Ontario, Canada.

E-Mail: salemaqeel@gmail.com

Prof. Dr. Nabil El-Faramawy (Egypt)

Research field: Radiation & Nuclear Physics and Dosimetry.

Position: Head of Physics Department, Faculty of Science, Ain Shams University, Cairo, Egypt.

Affiliation: Physics Department, Faculty of Science, Ain Shams University, Khalifa El-Maamon Street, 11566, Cairo, Egypt.

E-Mail: nabil_elfaramawi1@sci.asu.edu.eg ,
dr.na_bil@yahoo.com

Copyright © 2024 Thamar University

Prof. Dr. Levan Chkhartishvili (Georgia)

Research field: Semiconducting and Powder Composite Materials.

Position: Professor at the Department of Engineering Physics, Faculty of Informatics and Control Systems, Georgian Technical University, and researcher at F. Tavadze Metallurgy and Materials Science Institute, Semiconducting and Powder Composite Materials Laboratory.

Affiliation: Department of Engineering Physics, Faculty of Informatics and Control Systems, Georgian Technical University, 77 M. Kostava Ave., GTU Campus 4, Room 307, Tbilisi, 0160, Georgia.

E-Mail: levanchkhartishvili@gtu.ge , chkharti2003@yahoo.com

Prof. Dr. Saeed M. Al-Ghalibi (Yemen)

Research field: Bacteriology, Fungi, Medical microbiology, and Food Microbiology.

Position: Deputy Dean of Faculty of Science for Academic Affairs and Graduate Studies, Faculty of Science, Sana'a University, Sana'a, Yemen

Affiliation: Department of Biology, Faculty of Science, Sana'a University, Sana'a, Yemen.

E-Mail: s.alghalabi@su.edu.ye ,
Alghalibi@gmail.com

Prof. Dr. Abdulkarim A. Amad (Yemen)

Research field: Animal nutrition and production feed and feeding.

Affiliation: Faculty of Agriculture, Thamar University, Dhamar, Yemen and Institute of Animal Nutrition, Department of Veterinary Medicine, Frei Universität Berlin, Berlin, Germany.

E-Mail: abdulkarim.Amad@tu.edu.ye ,
abeerobeid@yahoo.com

Prof. Dr. Nabil M. Al-Areeq (Yemen)

Research field: Petroleum Geology, Hydrology, Sedimentology, Integrated Water Resources Management, Data analysis and Resolving of Water Related Conflicts.

Position: Centre Director of Water Resources and Environment, Thamar University, Dhamar, Yemen.

Affiliation: Department of Geology and Environment, Faculty of Applied Science, Thamar University, Dhamar, Yemen.

E-Mail: alareeqnabil@tu.edu.ye ,
nabilalareeq@yahoo.com

Prof. Dr. Ibrahim Radman Al Shaibani (Yemen)

Research field: Veterinary Parasitology.

Position: Vice Dean for students' affair, Faculty of Veterinary Medicine, Thamar University, Dhamar, Yemen.

Affiliation: Faculty of Veterinary Medicine, Thamar University, Dhamar, Yemen.

E-Mail: ibrahim.alshaibani@tu.edu.ye ,
dr_ibra67@yahoo.com

Prof. Dr. Salah Mahdi Saleem Al-Bader (Iraq)

Research field: Fungal taxonomy, Fungal ecology, and Natural products as antifungal agents.

Affiliation: Department of Medical Laboratory Sciences, College of Science, Knowledge University, Erbil, Iraq.

E-Mail: salah.mahdi@knu.edu.iq

Prof. Dr. Abeer Omer A. Obeid (Yemen)

Research field: Organic chemistry, Polymers, Liquid Crystals, and synthesis of heterocyclic compounds, as well as Anti-cancer and Antibacterial applications.

Affiliation: Department of Chemistry, Faculty of Science, Sana'a University, Sana'a, Yemen.

E-Mail: ab.obaid@su.edu.ye ,
abeerobeid@yahoo.com

Prof. Dr. Abduh M. Abdulwahab (Yemen)

Research field: Single Crystal, Crystal Structure, Physical Characterization of Solid-State Materials and Solid-State Physics.

Affiliation: Department of Physics, Faculty of Applied Sciences, Thamar University, Dhamar, Yemen.

E-Mail: abduh.abdulwahab@tu.edu.ye ,
abduhabdulwahab@yahoo.com

Prof. Dr. Omar M. A. Al Shuja'a (Yemen)

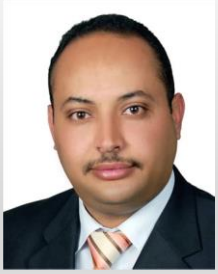

Research field: Materials Chemistry, Polymer Chemistry, and Physical Chemistry.

Position: Dean of the Center for Development and Quality Assurance, Al-Nasser University, Sana'a, Yemen.

Affiliation: Department of Chemistry, Faculty of Applied Sciences, Thamar University, Dhamar, Yemen.

E-Mail: omrshugaa@tu.edu.ye ,
abduhabdulwahab@yahoo.com

Assoc. Prof. AbdulSalam M. Al-Makdad (Yemen)

Research field: Diagnosis, management, and care of acute and chronic liver disease and GI diseases. Diagnostic and interventional GI endoscopy.

Position: President of the internal medicine department in AL-Wahda Teaching Hospital Maabar, Maabar City, Dhamar, Yemen.

Affiliation: Department of Internal Medicine, Faculty of Medicine, Thamar University, Dhamar, Yemen.

E-Mail: aalmakdad@tu.edu.ye

Assoc. Prof. Shaimaa A. A. Momen (Egypt)

Research field: Entomology.

Affiliation: Department of Entomology, Faculty of Science, Ain Shams University, Khalifa El-Maamon Street, 11566, Cairo, Egypt.

E-Mail: Shaimaa_momen@sci.asu.edu.eg ,
Shaimaa_momen@hotmail.com

Assoc. Prof. Essam A. Al-Moraissi (Yemen)

Research field: Oral and maxillofacial surgery, craniomaxillofacial trauma, temporomandibular joint disorders, orthognathic surgery, surgical pathology, cleft lip and palate, implant dentistry, lower third molar surgery, regenerative medicine, and adult mesenchymal stem cells.

Affiliation: Department of Oral and Maxillofacial Surgery, Faculty of Dentistry, Thamar University, Dhamar, Yemen.

E-Mail: dressamalmoraissi@tu.edu.ye

Assoc. Prof. Salah Abdul-Jabbar Jassim (Iraq)

Research field: Thin Films, Semiconductor Devices, and Solid-State Physics.

Affiliation: Department of Dentistry, AL Kunooze University College, Basrah, Iraq.

E-Mail: salah.abdul.jabbar@kunoozu.edu.iq ,
salahjassim200@yahoo.com ,
salah.jassim@alayen.edu.iq

Assoc. Prof. Amin Saif Ahmed (Yemen)

Research field: Energy and control systems engineering.

Affiliation: Department Mechatronics, Al-Saeed College of Engineering and Information Technology, Taiz University, Taiz, Yemen.

E-Mail: sameeralromima@yahoo.com , sameeralromima@gmail.com

Assoc. Prof. Dina Salah Eldin M. Abdelrhman (Egypt)

Research field: Gold Nanoparticles, Photochemistry, Nanotechnology, and Nanomedicine.

Affiliation: Biophysics, Physics Department, Faculty of Science, Ain Shams University, Khalifa El-Maamon Street, 11566, Cairo, Egypt.

E-Mail: dinasalah@sci.asu.edu.eg ,
dandy741@hotmail.com ,
dandy741@gmail.com

Assoc. Prof. Fawaz M. A. Al-Badaii (Yemen)

Research field: Microbiology, Antimicrobial resistance, Environmental Science, Heavy metals, and Adsorption Water quality.

Affiliation: Department of Biology, Faculty of Applied Sciences, Thamar University, Dhamar, Yemen.

E-Mail: fawaz.AlBadai@tu.edu.ye ,
abdualwhab1974@gmail.com

Assoc. Prof. Abdulwahab B. Alwany (Yemen)

Research field: Solid State Physics, Thein Films, Materials Science, and Nanoscience.

Affiliation: Department of Physics, Faculty of Science, Ibb University, Ibb, Yemen.

E-Mail: abdualwhab@yahoo.com ,
abdualwhab1974@gmail.com

Assoc. Prof. Ali Abdullah A. Al-Mehdar (Yemen)

Research field: Pharmacology & Therapeutics.

Affiliation: Department of Pharmacology and Toxicology, Faculty of Faculty of Medicine, Thamar University, Dhamar, Yemen.

E-Mail: ali.almehdar@tu.edu.ye , alialmehdar2006@yahoo.com

Assoc. Prof. Sameer A. M. Abdulrahman (Yemen)

Research field: Pharmaceutical Analytical Chemistry and Water Treatment.

Affiliation: Department of Chemistry, Faculty of Education and Sciences-Rada'a, Albaydha University, Albaydha 14517, Yemen.

E-Mail: sameeralromima@yahoo.com , sameeralromima@gmail.com

Copyright © 2024 Thamar University

Assoc. Prof. Nada M. Al-Hamdani (Yemen)

Research field: Histology, and Physiology, specializing in Endocrinology.

Affiliation: Department of Biology, Faculty of Science, Sana'a University, Sana'a, Yemen.

E-Mail: n.alhamdni@su.edu.ye ,
hamdaninadam@gmail.com

Assoc. Prof. Abdulbari A. A. Saeed (UK)

Research field: Preparation and characterization of mesoporous from solid waste as catalysis for water purification, Separation technology using an adsorption process, Water and wastewater treatment, and Biofuel production from organic solid waste.

Affiliation: School of Engineering, Institute for Infrastructure and Environment (IIE), University of Edinburgh, Edinburgh EH9 3JL, UK.

E-Mail: alborani_75@yahoo.co.uk , Abdulbari.Saeed@ed.ac.uk

Assoc. Prof. Yahya Qaid Hasan Ali (Yemen)

Research field: Differential Equations, Numerical Analysis, and Adomian Decomposition Method.

Affiliation: Department of Mathematics, Faculty of Applied Sciences, Thamar University, Dhamar, Yemen.

E-Mail: qaid.Yahya@tu.edu.ye ,
yahya217@yahoo.com

Assoc. Prof. Abdullah Alwarafi (Yemen)

Research field: Social Pharmacy.

Position: Vice Dean for Student Affairs, Faculty of Dentistry, Ibb University, Ibb, Yemen

Affiliation: Pharmacy Department, Faculty of Dentistry, Ibb University, Ibb, Yemen.

E-Mail: abdullahalwarafi@gmail.com , dentistry@ibbuniv.edu.ye

Prof. Dr. Ahmed A. M. Alakwa (Yemen)

Research field: Agricultural Economics.

Position: Head of Scientific Research, Vice Presidency of the University for Postgraduate Studies and Scientific Research, Thamar University, P O Box 87246 Dhamar, Yemen

Affiliation: Faculty of Agriculture, Thamar University, Dhamar, Yemen.

E-Mail: Hawali.ahmed@tu.edu.ye , alakwaahmed55@gmail.com

Prof. Dr. Ahmed Ali Saleh Obayeha (Yemen)

Research field: Orthodontics, Pediatric Dentistry, and Preventive Medicine.

Position: Dean of the Faculty of Dentistry, Al-Razi University, Sana’a, Yemen

Affiliation: Faculty of Dentistry Sana’a University, Sana’a, Yemen.

E-Mail: a.Obaya@su.edu.ye , Ahmedobeyah@yahoo.com

Assoc. Prof. Fathi Ahmed ELShawish (Yemen)

Research field: Identification and characterization of genetic sources of indigenous and introduced fruits, propagation and breeding of fruit crops, and design and layout of gardens.

Position: Deputy Dean for Postgraduate Studies and Scientific Research, Faculty of Agriculture, Thamar University, Dhamar, Yemen

Affiliation: Faculty of Agriculture, Thamar University, Dhamar, Yemen.

E-Mail: Fathi.ELShawish@tu.edu.ye ,

Assoc. Prof. Khalid Al-Hussaini (Yemen)

Research field: Information & Communication Technology (ICT), Computer Communications (Networks), Communication Engineering, and Computer Engineering.

Position: University Rector's Advisor for Academic Development & Automation and Vice Dean for Student Affairs, Faculty of Computer Science & Information Systems, Thamar University, Dhamar, Yemen.

Affiliation: Department of Information Technology, Faculty of Computer Science & Information System, Thamar University, Dhamar, Yemen.

E-Mail: khalid.alhussaini@tu.edu.ye

Assoc. Prof. Rasheed M. Alsanafi (Yemen)

Research field: Surveying & Urban Engineering and Planning, Civil Engineering.

Position: Postgraduate Studies and Scientific Research, Faculty of Engineering, Thamar University, Dhamar, Yemen.

Affiliation: Department of Civil Engineering Faculty of Engineering, Thamar University, Dhamar, Yemen.

E-Mail: alsanafy@tu.edu.ye , alsanafy@hotmail.com

Assoc. Prof. Kamal O. I. Ba'hakem (Yemen)

Research field: Surgical Gastroenterology, Upper & Lower GIT Endoscopy (diagnostic and therapeutic), Bleeding emergency GIT, Major conventional GIT surgery including biliary tree reconstructions, ERCP specialist, and General Surgeon.

Position: Vice director of AL-Wahda Teaching Hospital Maabar, Thamar University, Yemen.

Affiliation: Department of Surgery, Faculty of Medicine, Thamar University, Dhamar, Yemen.

E-Mail: mkamel1970@yahoo.com , khemo1970@gmail.com

Prof. Dr. Saad S. AL-Tobaili (Yemen)

Research field: Graph Theory and Mathematical Modeling relationships.

Affiliation: Department of Mathematics, Faculty of Science, Hadhramout University, Mukalla, Hadhramout, Yemen.

E-Mail: saadaltabili1@yahoo.com

Assoc. Prof. Fateh Abdo Ali Allahabi (Yemen)

Research field: Applied Mathematics, Control Theory, and Topology.

Affiliation: Department of Mathematics, Faculty of Applied Sciences, Thamar University, Dhamar, Yemen.

E-Mail: fateh.allahabi@tu.edu.ye , fateh74@gmail.com

Assoc. Prof. Hassan A. M. Al-Khawlani (Yemen)

Research field: Horticulture and Biotechnology.

Affiliation: Agriculture research & extension authority (AREA), Dhamar, Yemen.

E-Mail: alkholanihassaan@gmail.com

Assoc. Prof. Amin M. A. AlWaseai (Yemen)

Research field: Biotechnology and Food Technology.

Position: Head of Biotechnology & Food Technology Department, Faculty of Agriculture, Thamar University, Dhamar, Yemen.

Affiliation: Department of Biotechnology & Food Technology, Faculty of Agriculture, Thamar University, Dhamar, Yemen.

E-Mail: amin.alwaseai@tu.edu.ye , amin_alwaseai2000@yahoo.com

Technical Team

Technical Editing by:

Mr. Mohammed Subaie

Volume 9, Issue 2, December 2024

Articles

Thamar University Journal of Natural & Applied Sciences **9**(2) (2024) 1–5

DOI: https://doi.org/10.59167/tujnas.v9i2.2308

TUJNAS

Original Article

New approach for calculating nuclear binding energies of nickel isotopes $^{57-78}_{28}Ni$ by using the Shell Model

Nawras Ghazi Alhoulami

Department of Physics, Faculty of Science, Al Furat University, Deir-ez-Zor, Syrian Arab Republic.

Corresponding author: Nawras G. Alhoulami, email: E-mail: nawrasalhoulami@alfuratuniv.edu.sy

Received: 11 April 2024. Received (in revised form): 17 May 2024. Accepted: 21 May 2024. Published: 26 December 2024

Abstract

Depending on the basic assumptions of the Shell Model and by using suitable potentials, we found a new formula to calculate the nuclear binding energies of nickel isotopes $^{57-78}_{28}Ni$. This formula is related only to the mass number of these isotopes and the number of valence nucleons outside the closed core $^{56}_{28}Ni$. When calculating the standard deviation of the experimental data from the theory, we found that our value is better than the value calculated by the Semi-Empirical Mass Formula; it is also better than that calculated by the Integrated Model and calculated by the Modified Integrated Model. This indicates that our inferred formula is better than the most important formulas previously used to calculate nuclear binding energies for our studied nuclei.

Keywords: Nuclear Binding Energy; Valence Nucleons; Shell Model; Closed Core.

1. Introduction

One of the most important purposes of nuclear physics is to provide nuclear models that explain the properties and behavior of atomic nuclei. One of the most important nuclear properties is that the density of the nucleus is almost constant, so the size of the nuclei is proportional to their mass number [1].

We find that the same applies to liquids, so one of the first nuclear models was the Liquid Drop Model (LDM), which was presented by Carl Friedrich Von Weizsacker in 1935 and Bohr established its basic hypotheses [2].

Depending on this model, the values of the nuclear binding energies of the nuclei were calculated using the Semi-Empirical Mass Formula (SEMF), which is known as the Bethe-Weizsäcke formula [3]. In 2011, a new formula was developed to calculate the values of the nuclear binding energies, which was deduced by Nader Ghahramany and his group [4]. This relation is based on the theory of Quantum Chromodynamics, where nuclear matter is treated as a plasma composed of a soup of quarks and gluons. This formula is called the Integrated Nuclear Model (INM). Hezekiah K. Cherop and Kapil M. Khanna [5] developed this formula in 2020, and it is called the Modified Integrated Nuclear Model (MINM).

In these nuclear models, nucleons are not dealt with separately but rather as a static system. Therefore, these models succeeded in calculating some properties of nuclei, such as the average nuclear binding energy for each nucleon, while they failed to calculate other nuclear properties, such as excited states and magnetic moments.

On the other hand, the Shell Model developed by Mayer and Jensen was proposed in 1948[6] on the assumption that each nucleon in any nucleus moves independently in a median potential resulting from the rest of the nucleons, which is called the valance field, expressing a "central field.". This field, in addition to potential resulting from the mutual effects between each of the two nucleons of the nucleons, is called the residual potential. According to this model, nucleons are located on separate energy levels called single-particle levels, which are determined by solving the Schrödinger equation by choosing an appropriate potential. This model succeeded in calculating many nuclear properties, such as predicting magic numbers, spin-parity, predictive power of excited states for nuclei remote from the doubly magic nuclei, and their magnetic moments, but it did not give good value for the nuclear binding energies for most of the nuclei especially far from the stability line. Therefore, in this study, we found a new formula to calculate the values of nuclear binding energy in the function of the mass number and the number of valence nucleons when they are in the ground state, depending on the basic assumptions of the Shell Model and the selection of suitable potentials. We calculated the values of the nuclear binding energies by this new approach of all the isotopes of nickel odd (even - odd) and even (even - even), whose valence nucleons are located between the two magic numbers, $28 < N \leq 50$.

2. Nuclear Shell Model

The basic assumption of the nuclear shell model is that, to a first approximation, each nucleon moves independently in a potential that represents the average interaction with the other nucleons in a nucleus. This independent motion can be qualitatively understood from a combination of the weakness of the long-range nuclear attraction and the Pauli exclusion principle.

In a non-relativistic approximation, nuclear properties are described by the Schrodinger equation for A nucleons [7], i.e.:

$$\hat{H}|\Psi\rangle = E|\Psi\rangle \qquad (1)$$

where Ψ is an A-body wave function, and $\hat{H}$contains nucleon kinetic energy operators and interactions between nucleons of a two-body and a three-body character; in the present study, we will consider only the two-body interaction, i.e.:

$$\hat{H} = \sum_{i=1}^{A}(-\frac{\hbar^2}{2m}\Delta_i) + \sum_{i<j=1}^{A} W(i,j) \tag{2}$$

We can re-write the Hamiltonian (2), adding and subtracting a one-body potential of the form of $\sum_{i=1}^{A} U(i)$ as [7]:

$$\hat{H} = \sum_{i=1}^{A}[-\frac{\hbar^2}{2m}\Delta_i + U(i)] + \sum_{i<j=1}^{A} W(i,j) - \sum_{i=1}^{A} U(i) = \hat{H}^{(0)} + \hat{H}^{(1)} \tag{3}$$

where $\hat{H}^{(0)}$ is the zero Hamiltonian, a sum of single-particle Hamiltonians that expresses the average potential of all nucleons.

$$\hat{H}^{(1)} = \sum_{i<j=1}^{A} W(i,j) - \sum_{i=1}^{A} U(i) \equiv V$$

is called a *residual interaction.*

It is clear that when the number of nucleons is large, the Hamiltonian matrix becomes very large, so we use an approximating valence space or model space [8], which consists of all single-particle orbitals actively involved in the generation of configurations of the many-nucleon system considered, and assumes the existence of a closed core is the closest doubly magic nucleus to the studied nucleus. Therefore, the study is limited to valence nucleons (the nucleons that lie outside the closed core) instead of being between all nucleons.

The reason for defining a core is that the computational effort increases rapidly, with an increasing number of single-particle orbitals induced in the valence space.

We can re-write the Hamiltonian (3) according to the Valance Space as [8]:

$$\hat{H} = E(CORE) + \bar{\varepsilon}(\hat{n})\hat{n} + \sum_{i=1}^{A} U(i) + \hat{H}^{(1)} \tag{4}$$

where $E(CORE) = -BE(CORE)$ is the nuclear binding energy of the closed core, $\bar{\varepsilon}$ the average nuclear binding energy of valance nucleons, and $\hat{n}$is the particle number operator. Now will describe how each term of this equation was calculated.

2.1. Average nuclear binding energy of valance nucleons $\bar{\varepsilon}$

We can obtain the value of average binding energy for each valence nucleon in the ground state by best fitting for the experimental single-particle energies [9]. The valence nucleons in our study fall within the pfgshell, outside the closed core $^{56}_{28}Ni$, which have the following valence levels, respectively [10]:

$$1p_{3/2} = -10.25MeV, 0f_{5/2} = -9.48MeV, 1p_{1/2} = -9.14MeV, 0g_{9/2} = -6.55MeV$$

By performing the best fitting (using the LAB fit program), we got the best form of the equation which represents the average energy of a single particle in the valence levels in terms of the number of valence nucleons, which takes the following form:

$$\bar{\varepsilon}(\hat{n}) = a + b\hat{n}(MeV) \tag{5}$$

where a and b constants that take the following values:

$$a = \text{-}10.94MeV, b = 0.2323MeV$$

2.2. Mean Field Potential

It is the central potential produced by all valence nucleons so that each nucleon of the valence nucleons is moving independently in this central potential resulting from the rest of all the nucleons.

This potential can take different forms, such as the Harmonic Oscillator, Woods-Saxon potential, and Paring potential.

Assuming that the valence nucleons are all in the ground state and are paired with each other, the most appropriate potential to describe this system is the Paring potential, which takes the following form [11]:

$$V_{PAIR} = -G\sum_{\rho} A_{\rho}^{+} A_{\rho} \tag{6}$$

where $A_{\rho}^{+} = \sum_{i=1}^{p} A_{\rho}^{+}(i)$ and $A_{\rho} = \sum_{i=1}^{p} A_{\rho}(i)$is pair creation operators and ρ is the number of j-orbits in the mean-field considered, and $G > 0$ is an isovector paring strength, which is given in terms of mass number as follows $G = \frac{20}{A}$[9, 12].

Depending on paring potential, paring energy when all the nucleons are in the ground state is given by the following equation [8]:

$$E_{\nu}(N) = -\frac{1}{4}G(N-\nu)(2\Omega - N - \nu + 2) \tag{7}$$

where ν is the Seniority quantum number, which is the number of nucleons not pairwise coupled to angular momentum zero; in short, the number of unpaired nucleons, Nindicates the number of nucleons in the ground state (which represents the number of valence nucleons in our study), and Ω indicates the maximum number of paired pairs that a given level fits into nucleons; it is given by $\Omega = \frac{1}{2}(2j+1)$.

Increasing the number of neutrons$N$over the number of protons$Z$in the nucleus, it decreases their stability. It thus decreases their total nuclear binding energy, so we will add another term to mean field potential (Paring potential) that results from the Symmetry Effect, which takes the following equation [13]:

$$V_{sym} = \sum_{1,2} \frac{t_1 . t_2}{A} V_1 V_1 \approx 100(MeV) \tag{8}$$

where $t_1$and t_2 are the isospin for two nucleon interactions. Depending on the previous Symmetry potential, the energy from this potential is given by the following equation:

$$E_{Asy} = (N-Z)\frac{V_1}{A} \tag{9}$$

In our study, the amount $(N-Z)$ represents the number of valence nucleons outside the closed core.

2.3. Residual Interaction $\hat{H}^{(1)}$

The effect of the residual interaction is only between valence nucleons, and its contribution to the total Hamiltonian is small compared to the mean field potential, so it is treated as a perturbation, and this interaction takes different forms. In this study, we chose the Surface Delta Interaction (SDI) because it is easy to deal with and has a separable potential, which allows obtaining an analytical solution to the Schrödinger equation. This form of interaction was postulated in 1966 by Moszkowski *et.al.* [14]. This is based on the Pauli principle, which is forbidden when collisions occur at the full levels and allows collisions to occur mainly at the valance levels. This interaction was developed by Glaudesmans [15], and is called Modified Surface Delta Interaction (MSDI). The matrix element of residual interaction for one of the interacting valence-nucleon pairs is as follows:

$$\begin{aligned}
&\langle j_a j_b, JT|V_{\mathrm{MSDI}}|j_c j_d, JT\rangle_{JT} \\
&= \frac{A_T}{2(2J+1)}\left[\frac{(2j_a+1)(2j_b+1)(2j_c+1)(2j_d+1)}{(1+\delta_{ab})(1+\delta_{cd})}\right]^{\frac{1}{2}}\{(-1)^{\ell_a+\ell_c+j_b+j_d}(j_b \\
&- \frac{1}{2}j_a\frac{1}{2}|J0) \\
&(j_d - \frac{1}{2}j_c\frac{1}{2}|J0)[1-(-1)^{\ell_c+\ell_d+J+T}] - (j_b\frac{1}{2}j_a\frac{1}{2}|J1)(j_d\frac{1}{2}j_c\frac{1}{2}|J1)[1 \\
&\qquad + (-1)^T]\} \\
&\qquad + B_T[2T(T+1)-3]\delta_{ac}\delta_{bd}
\end{aligned} \tag{10}$$

where A_T,B_T is two constants represent the strength interaction of MSDI. The symbol $(j - \frac{1}{2}j\frac{1}{2}|J0)$ indicates to Clebsch-Gordan coefficients, and j is the angular momentum of the nucleon, and J is the total angular momentum of two nucleon interaction, and the symbol T refers to total isospin produced by the isospin coupling of the two interacting nucleons. When the valence nucleons are in the ground state, the formula (10) turns out to be:

$$\langle j_a j_b, JT | V_{MSDI} | j_a j_b, JT \rangle_{JT} = -A_T \frac{(2j_a+1)(2j_b+1)}{2(2J+1)(1+\delta_{ab})} \{ \left[(j_a \tfrac{1}{2} j_b - \tfrac{1}{2} | J0) \right]^2 [1 - (-1)^{\ell_a+\ell_b+J+T}] + \left[(j_b \tfrac{1}{2} j_a \tfrac{1}{2} | J1) \right]^2 [1 + (-1)^T] \} + B_T [2T(T+1) - 3] \tag{11}$$

When the two valence nucleons fall within the same level, the previous formula becomes as follows:

$$\langle j^2, J1 | V_{MSDI} | j^2, J1 \rangle_{JT=1} = A_T \frac{(2j+1)^2}{2(2J+1)} (j - \tfrac{1}{2} j \tfrac{1}{2} | J0)^2 + B_T \tag{12}$$

If the valence nucleons are pairwise coupled to angular momentum zero, the previous formula becomes after the parameter, Ω, is substituted as follows:

$$\langle j^2, 01 | V_{MSDI} | j^2, 01 \rangle_{J=0T=1} = \frac{1}{2} A_T (2j+1) + B_T = A_T \Omega + B \tag{13}$$

We have benefited from the following transformation [8]:

$$(jmjm'|00) = (-1)^{j-m} \hat{j}^{-1} \delta_{m,-m'} \tag{14}$$

The value of the MSDI strengths can be obtained by fitting with the empirical values, and it is also approximated in terms of mass number as follows $A_T \approx B_T \approx \frac{25}{A} MeV$ [16], so we can rewrite the formula (13) as:

$$H^{(1)} \equiv \langle j^2, 01 | V_{MSDI} | j^2, 01 \rangle_{J=0T=1} = \frac{25}{A} (\Omega + 1) \tag{15}$$

The previous formula can also be written in terms of isovector paring strength as follows:

$$H^{(1)} \equiv \langle j^2, 01 | V_{MSDI} | j^2, 01 \rangle_{J=0T=1} = 1.25 G (\Omega + 1) \tag{16}$$

3. Calculations and Results

The nuclear binding energies were calculated for the twenty-two nuclei of nickel isotopes that lie outside the closed core $^{56}_{28}Ni$, related to the following mass numbers $A = 57 - 78$. Eleven nuclei of them are odd (even - odd), and eleven nuclei are even (even - even) depending on the new formula (4), and that is after compensating the equations (5), (7), (9) and (16) in them, and making some reforms to take the following form:

$$E = -BE = E(CORE) + C_1 n^2 + C_2 n + C_3 \tag{17}$$

where $E(CORE) = -BE(^{56}_{28}Ni) = -483.98811(MeV)$ [17] , C_1,C_2 and C_3 takes the following values.

$$C_1 = b + \frac{1}{4} G, C_2 = a - \frac{1}{2} G(\Omega + 11), C_3 = \frac{G}{4} \{ \nu (2\Omega - \nu + 2) + 5(\Omega + 1) \} \tag{18}$$

When the nucleons are in the ground state, the seniority quantum number takes $\nu = 0$ for even-even nuclei and the value $\nu = 1$ for even-odd nuclei [8].

Since the Ω indicates the maximum number of pairs of nucleons that each level of the shell pfg accommodates, so in our case, it takes specific values as follows:

$$\Omega = \begin{cases} 2 for A = 57 \rightarrow 60 \\ 3 for A = 61 \rightarrow 66 \\ 1 for A = 67 \rightarrow 68 \\ 5 for A = 69 \rightarrow 77 \end{cases} \tag{19}$$

The value of the isovector paring strength G can be obtained by fitting with the experimental nuclear binding energies, and its value can also be obtained in terms of mass number, then the parameter C_1,C_2 and C_3 will be

$$C_1 = b + \frac{5}{A}, C_2 = a - \frac{10}{A} (\Omega + 11), C_3 = \frac{5}{A} \{ \nu (2\Omega - \nu + 2) + 5(\Omega + 1) \} \tag{20}$$

Applying the formula (17) to the isotopes of nickel $^{57-78}_{28}Ni$ using the given parameters in the equation (20). We get the nuclear binding energies of these isotopes $B_{SM}(MeV)$ which are shown in Table 1 compared with the values of the experimental binding energies $B_{exp.}$[17]

Table 1: The nuclear binding energies of our calculated nickel isotopes $^{57-78}_{28}Ni$ compared with the experimental values.

Even-Odd- A				**Even- Even-A**			
A	$B_{SM}(MeV)$*	$B_{exp.}$	$\|B_{SM} - B_{exp}$	A	$B_{SM}(MeV)$*	$B_{exp.}$	$\|B_{SM} - B_{exp}\|$
57	495.1413	494.2430	0.8983	**58**	507.7906	506.4590	1.3316
59	518.8768	515.4580	3.4188	**60**	530.1215	526.8460	3.2755
61	540.1006	534.6660	5.4346	**62**	550.3045	545.2620	5.0425
63	558.7161	551.3840	7.3321	**64**	567.5853	561.7570	5.8283
65	574.7156	567.8550	6.8606	**66**	582.2862	576.8080	5.4782
67	585.9282	582.6150	3.3132	**68**	591.6767	590.4080	1.2687
69	601.8838	594.9940	6.8898	**70**	607.4813	602.3000	5.1813
71	610.8979	606.5640	4.3339	**72**	615.2606	613.4550	1.8056
73	617.4978	617.4090	0.0888	**74**	620.6498	623.8280	3.1782
75	621.7280	627.6890	5.9610	**76**	623.6908	633.1240	9.4332
77	623.6284	636.3330	12.7046	**78**	624.4213	641.7870	17.3657

*The values of our calculated nuclear binding energy (in black) compared to the experimental values (in red) are shown in Figure 1.

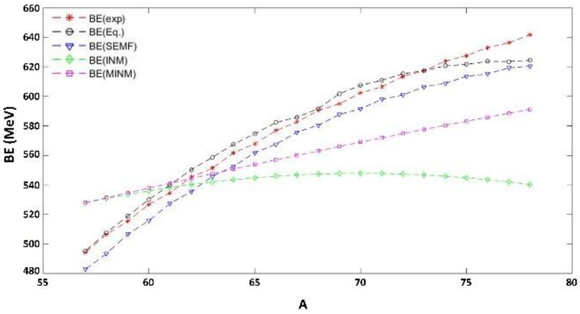

Figure 1: nuclear binding energies of our computed nickel isotopes $^{57-78}_{28}Ni$ (in black) and calculated using the Semi-Empirical Mass Formula (in blue), computed using the Integrated Model (in green) and computed using the Modified Integrated Model (in pink) compared to the experimental values (in red).

When we calculate the standard deviation between our nuclear binding energy values for the studied nuclei and the experimental values, we used the following standard deviation equation:

$$\sigma = \sqrt{\frac{1}{N}\sum_{i=1}^{N\sum}\left[[BE^{i}_{SM} - BE^{i}_{exp.}]^2\right]} \tag{21}$$

We found that the standard deviation for the studied nuclei is $\sigma = 6.5758$ (MeV), where a value $\Delta B = |B_{eq.} - B_{exp}$ for each studied nuclei is shown (in black) in Figure 2.

When calculating nuclear binding energies for the studied nuclei using the Semi-Empirical Mass Formula, which is the most popular formula for finding nuclear binding energies, which is given as follows [3]:

$$BE = a_V A - a_S A^{\frac{2}{3}} - a_C \frac{Z^2}{A^{\frac{1}{3}}} - a_{AS}\frac{(A-2Z)^2}{A} \pm \delta \tag{22}$$

where $a_V, a_S, a_C, a_{AS}, \&\ a_p$ are the coefficients in the Semi-Empirical Mass Formula, which takes many sets of values; we chose the most common and used ones, which are [18]:

$$a_V = 15.78(MeV), a_S = 18.34(MeV), a_C, = 0.71(MeV), a_{Sym} = 23.21(MeV),$$

$$a_p = \begin{cases} 12(MeV) for even - even \\ 0 for odd - even \end{cases}$$

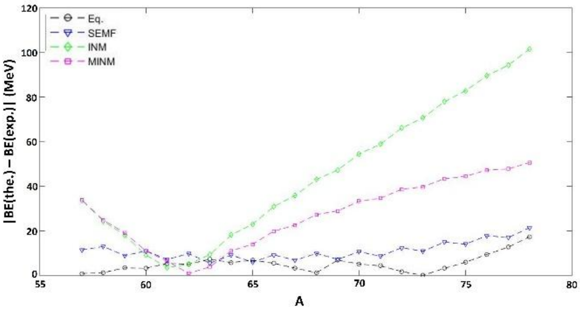

Figure 2: Values for our calculated nickel isotopes $^{57-78}_{28}Ni$ (in black), calculated using the Semi-Empirical Mass Formula (in blue), calculated using the Integrated Model (in green), and computed using the Modified Integrated Model (in pink).

The nuclear binding energies calculated by the Semi-Empirical Mass Formula are shown (in blue) in Figure 1. We found the standard deviation calculated using the Semi-Empirical Mass Formula for the nuclei we studied is$\sigma = 11.7440(MeV)$, where the value $\Delta B(MeV)$ of these nuclei is shown (in blue) in Figure 2.

When we calculate the nuclear binding energies of the studied nuclei using the Integrated Model, which is given by the following formula [4]:

$$BE(A,Z) = \left[3A - \left(\frac{(N^2 - Z^2) + \delta(N-Z)}{Z}\right) + 3^2\right]\frac{m_u c^2}{100}, for\ A > 5 \tag{23}$$

where $m_u c^2 = 330\ (MeV)$ is nucleon mass, and the parameter δ is related to the stability of the nuclei against the beta decays and takes the following two values:

$$\delta(N-Z)\begin{cases} 0 for N \neq Z \\ 1 for N = Z \end{cases}$$

where the nuclear binding energies of the studied nuclei calculated by the previous formula are shown (in green) in Figure 1. We found that the standard deviation value calculated for the studied nuclei by the Integrated Model formula is $\sigma = 54.5307\ (MeV)$, where the value $\Delta B(MeV)$ calculated with this formula is shown (in green) in Figure 2.

When we calculate the nuclear binding energies for the studied nuclei using Modified Integrated Model, which are given as follows [5]:

$$BE(A,Z) = \left[3A - \left(\frac{(N^2 - Z^2) + \delta(N-Z)}{\sqrt{NZ}}\right) + \lambda\right]\frac{m_u c^2}{100}, for\ A > 5 \tag{24}$$

where the parameter λ is taken for $Z \leq 30$ the constant value $\lambda = 9$.

The nuclear binding energies of the studied nuclei calculated by the previous formula are shown (in pink) in Figure 1. We found that the standard deviation value calculated for the studied nuclei by the Modified Integrated Model formula is $\sigma = 31.2226\ (MeV)$, where the value $\Delta B\ (MeV)$ calculated with the last formula is shown (in pink) in Figure 2.

4. Conclusion

Depending on the basic assumptions of the Shell Model and using suitable potentials, we found a new simple formula to calculate the nuclear binding energy in the function of the mass number and the number of valence nucleons.

We calculated by this formula the nuclear binding energies of twenty-two nuclei of nickel isotopes, eleven of which are even-odd and eleven even-even nuclei whose valence nucleons are located outside the closed core $^{56}_{28}Ni$ which have a valence nucleon located between the two magic numbers $28 < N \leq 50$.

We found the standard deviation between our calculated nuclear binding energies and the experimental values is better than the value calculated by the Semi-Empirical Mass Formula, and it is also better than the value calculated by the Integrated Model and calculated by the Modified Integrated Model. This indicates that our deduced formula is better than the most important formulas previously used to calculate the nuclear binding energies of the studied isotopes of nickel.

We expect an improvement in the values of the nuclear binding energies of the studied nuclei compared to the experimental values when taking the residual interaction between all valence nucleons; we also expect an improvement in the values when adding another term to the mean field potential related to the deformation of the nucleus, especially when the number of valence nucleons increases significantly outside the closed core, as in the case of the last three isotopes $^{76,77,78}_{28}Ni$.

After determining the form of the equation for the average nuclear binding energy of valence nucleons, we suggest studying the possibility of applying the formula used in this study to other areas of nuclei. We also suggest studying the possibility of using this formula to calculate the excitation energy of the nuclei.

Data Availability

The datasets used and analyzed during the current study are available from the corresponding author upon reasonable request.

Conflict of Interest

The authors declare no conflict of interest.

References

[1] Basdevant, J.-L., Rich, J., Spiro, M. (2005) Fundamentals in nuclear physics: From nuclear structure to cosmology, 1st ed., Springer Science & Business Media, New York, USA, pp. 500-515.

[2] Von Weisslcker, C. (1935) Sur Theorie der Kernaassen, *Zeitschrift für Physik* **9**: 431-458.

[3] Benzaid, D., Bentridi, S., Kerraci, A., Amrani, N. (2020) Bethe–Weizsäcker semiempirical mass formula coefficients 2019 update based on AME2016, *Nuclear Science and Techniques* **31**: 9.

[4] Ghahramany, N., Gharaati, S., Ghanaatian, M., Hora, H. (2011) New scheme of nuclide and nuclear binding energy from quark-like model, *Iranian Journal of Science* **35**: 201-208.

[5] Cherop, H.K., Khanna, K.M. (2020) Modified integrated nuclear model for the binding energy of finite nuclei, *World Scientific News* **149**: 36-51.

[6] Mayer, M.G. (1950) Nuclear configurations in the spin-orbit coupling model. i. empirical evidence, *Physical Review* **78**: 16.

[7] Heyde, K.L.G., The Nuclear Shell Model, in: Heyde, K.L.G., (Ed.), Book (1994) The Nuclear Shell Model, Springer Berlin Heidelberg, Berlin Heidelberg, Germany, pp. 58-154.

[8] Pan, F., Qi, C., Dai, L., Sargsyan, G., Launey, K.D., Draayer, J.P. (2020) On the importance of np-pairs in the isovector pairing model, *Europhysics Letters* **132**: 32001.

[9] Suhonen, J. (2007) From nucleons to nucleus: concepts of microscopic nuclear theory, ed., Springer Science & Business Media, Berlin Heidelberg, Germany, pp. 400-500.

[10] Grawe, H., Shell Modelfrom a Practitioner's Point of View, in: Al-Khalili, J., Roeckl, E., (Ed.), Book (2004) Shell Modelfrom a Practitioner's Point of View, Springer Berlin Heidelberg, Berlin Heidelberg, Germany, pp. 33-75.

[11] Miora, M., Launey, K., Kekejian, D., Pan, F., Draayer, J. (2019) Exact isovector pairing in a shell-model framework: Role of proton-neutron correlations in isobaric analog states, *Physical Review C* **100**: 064310.

[12] Macchiavelli, A.O., Fallon, P., Clark, R.M., Cromaz, M., Deleplanque, M.A., Diamond, R.M., Lane, G.J., Lee, I.Y., Stephens, F.S., Svensson, C.E., Vetter, K., Ward, D. (2000) Is there np pairing in N = Z nuclei?, *Physical Review C* **61**: 041303.

[13] Bertsch, G.F., Mekjian, A. (1972) Isospin Impurities in Nuclei, *Annual Review of Nuclear and Particle Science* **22**: 25-64.

[14] Arvieu, R., Moszkowski, S.A. (1966) Generalized Seniority and the Surface Delta Interaction, *Physical Review* **145**: 830-837.

[15] Glaudemans, P.W.M., Brussaard, P.J., Wildenthal, B.H. (1967) Two-body matrix elements from a modified surface delta interaction, *Nuclear Physics A* **102**: 593-601.

[16] Shatha, F. (2005) Calculation of Energy Levels for Nuclei (42Ca, 42Ti, 42Sc) by using Modified Surface Delta Interaction. *Physics*, M. Sc. Thesis, Kufa University, Kufa, Iraq.

[17] NRV Nuclear Map. (1989-1999) *NRV Web Knowledge Base on Low-energy Nuclear Physics*. Russian Foundation for Basic Research http://nrv.jinr.ru/nrv/webnrv/map/

[18] Chowdhury, P.R., Samanta, C., Basu, D. (2005) Modified Bethe–Weizsäcker mass formula with isotonic shift and new driplines, *Modern Physics Letters A* **20**: 1605-1618.

Thamar University Journal of Natural & Applied Sciences ***9***(2) (2024) 6–9

DOI: https://doi.org/10.59167/tujnas.v9i2.2309

TUJNAS

Original Article

Studying the effect of soil factors on some anatomical and morphological properties of Olive *(Olea europaea L.)* leaves

Hiyam Jamal Ibrahim*, Ann Ahmed Sedeeq, and Israa Hawyyiz Kareem

Biology Department, College of Education for Pure Sciences, University of Kirkuk, Kirkuk, Iraq.

*Corresponding author: Hiyam Jamal Ibrahim, E-mail: Plantanatomy@uokirkuk.edu.iq

Received: 7 June 2024. Received (in revised form): 8 August 2024. Accepted: 12 August 2024. Published: 26 December 2024

Abstract

The current study aimed to evaluate the effect of soil factors on some characteristics of olive leaves. The beginning of the process was collecting plant and soil samples from some home gardens and public street gardens in the City of Kirkuk to conduct tests related to plants and soil. We performed Some tests on the soil to evaluate each type of soil and some properties of olive leaves from different sites. The present study showed differences in physical and chemical properties between the soil collected from home gardens and the soil collected from public street gardens. The electrical conductivity, total dissolved solids, sulfate, and dissolved potassium were higher in the soil collected from Public Street Gardens. In contrast, total nitrogen, phosphorus, calcium, magnesium, and organic matter values were higher in the soil collected from home gardens than in public street gardens. For leaf properties, the results show a significant ($P \leq 0.05$) decrease in average leaf area, Leaf dry matter, and Leaf ash in leaves collected from public street gardens compared to olive leaves collected from home gardens. For the structural characteristics of the leaf, the vascular cylinder, cuticle layer, mesophyll, and epidermis were smaller in the leaves of the group from Home Gardens than the leaves of the Public Street Gardens group. In contrast, the leaf edge and thickness were more significant in the leaves from home gardens than in public street gardens.

Keywords: *Olea europaea L.*; Soil Properties; Anatomical Properties; Morphological Properties.

1. Introduction

The olive (*Olea europaea L.*), a long-lived evergreen tree in the Oleaceae family, is one of the most extensively grown and significant fruit crops in terms of international trade. Native to every Mediterranean nation, olive trees are a vital component of the so-called Mediterranean diet [1-3]. Nineveh, Kirkuk, Baghdad, Erbil, and Duhok are among the cities in central and northern Iraq where olive trees are cultivated [4]. Olive fruit is significant because of its high nutritional value and caloric content. It is rich in minerals (K, Ca, Mg, and P) and vitamins (A, B, C, D, E, and K) [4-6]. Olive trees tolerate harsh environments and are often planted on steep hillsides with poor soil [7]. According to research by García-Orenes *et al.* [8-10], insufficient management practices are the primary cause of erosion in olive orchards aside from environmental variables. According to Espejo-Pérez *et al.* [7], eliminating naturally occurring vegetation between olive trees to lessen the competition between the weeds and the olive trees for light, water, and nutrients makes the soil more prone to erosion. Numerous variables contributing to soil degradation, including compaction, leaching, wind, and water erosion, threaten soil resources. One of the main factors contributing to land degradation globally is water erosion. Because the surface layer, typically the most fertile layer where organic matter and nutrients required for plant development are concentrated, is lost due to water erosion, soil quality is impacted. Degradation is induced [11-13]. When nutrients are supplied to leaves, they are often absorbed more quickly than when administered to soil. The characteristics of the soil strongly influence nutrient availability. For example, because clay soils tend to have high K-fixing capacities, most available K is quickly attached to the clay particles, meaning they often do not react well to K fertilizers added to the soil [14, 15]. Therefore, the current study aimed to evaluate the effect of soil factors on some characteristics of olive leaves.

2. Materials & Methods

2.1 Samples Collection

Collecting plant and soil samples from (ten locations) home gardens, and public street gardens in the city of Kirkuk began, and three samples were taken from each area to conduct tests related to plants and soil.

2.2 Physical and chemical factors measurement

2.2.1 Total Dissolved Solid (TDS)

It was measured in the field using a TDS meter, and the measurement was repeated twice for each sample in milligrams per liter (mg/L) or parts per million (ppm).

2.2.2 Electrical Conductivity (EC)

The electrical conductivity was measured in the field with an EC-meter in Siemens per meter (S/m) or mho and is usually represented by the Greek letter sigma, σ, after regulating the device using distilled water and adjusting the temperature to 25 °C.

2.2.3 pH

The acid function was measured using a pH meter after regulating it with buffer solutions.

2.2.4 Total nitrogen

The Kjeldahl method was used, according to the method described in [16], to estimate the percentage of total nitrogen in the samples.

2.2.5 Determination of phosphorus

This method is based on the reaction of phosphorus with vanadate and molybdate, which forms a yellow complex compound in acidic environments and is measured in the nm [17].

2.2.6 Potassium and calcium

Concentrations of potassium and calcium in soil samples were estimated using a FLAM device [18].

2.2.7 Sulphate Ion Concentration

Sulfate ions were estimated for the samples using the turbidimetric method, which included taking a known volume of the filtered sample measured in the mg/L [19].

2.2.8 Organic matter

The organic content values of soil samples were estimated according to what was stated in [20].

2.2.9 Soil texture

The soil texture measurement method is used to estimate the following proportions (clay, silt, and sand) using the pipette method measured in mm [20].

2.2.10 Leaf Properties

Average leaf area (cm^2) for the fifth leaf from the apex of twenty-one-year-old, non-fruiting shoots (selected randomly) in all directions of each tree. The leaves were obliterated and collected in polyethylene bags; then, their areas were measured using a leaf area meter (Model AM100, ADC Bioscientific Ltd.). Leaf Dry matter % (Total solids) calculated as (Determined Dm.% = 100 – moisture %). The ash % of leaves was determined by a muffle furnace at 450 °C for 4 hours, according to [21].

2.2.11 Anatomical Study

The epidermis was studied from the leaves of fresh specimens collected from the field immediately after they were fixed with a Formalin-Acetic Acid-Alcohol (F.A.A) solution, and a mixture of formalin-acetic acid-alcohol prepared by the method was measured in the µm [22].

2.2.12 Statistical Analysis

Statistical analysis of the data was conducted using the Special Program for Statistical Systems (SPSS, 2011). The statistical analysis was performed by applying the Linear Regression test, which is used to clarify the relationships between some of the studied variables (physical characteristics and chemical) and predict the value of one of the variables (The dependent variable) through the values of the other variable (the independent variable). This analysis model estimates the coefficients of the linear equation that includes one or more independent variables that best predict the value of the dependent variable. Also, the Pearson correlation coefficient was applied to some of the studied variables, a test to measure the relationship between Statistics or the correlation between two continuous variables.

3. Results & Discussion

3.1 Soil

The current study showed differences in physical and chemical properties between the soil collected from home gardens and the soil collected from public gardens. It was found that the electrical conductivity, total dissolved solids, sulfate, and dissolved potassium were higher in the soil collected from public street gardens. In contrast, total nitrogen, phosphorus, calcium, magnesium, and organic matter values were higher in the soil collected from home gardens compared to public garden soil in the streets, as shown in Tables 1 and 2.

Table 1: Some physical and chemical properties of soil collected from home gardens.

Location **Tests**	**1**	**2**	**3**	**4**	**5**
Electrical conductivity (EC)	0.126	0.165	0.134	0.159	0.171
pH	6.4	6.1	6.2	6.7	6.5
Total dissolved solid (TDS)	60	76	58	63	81
Total nitrogen	0.084	0.056	0.059	0.082	0.067
Phosphorus	18.818	19.8	13.014	12.18	17.31
Dissolved potassium	105.957	101.678	96.241	112.786	89.679
Sulphate	48.337	54.389	61.045	39.782	34.976
Calcium	28.399	31.525	37.818	40.977	33.656
Magnesium	9.450	8.786	10.831	12.324	14.306
organic matter	3.277	3.221	3.301	3.345	2.876
Texture	Sand loam	Sand loam	Sand loam	Sand loam	Sand loam
Clay	12	14	9	7	15
Silt	10	7	11	11	9
Sand	78	74	60	80	65

Table 2: Some physical and chemical properties of soil collected from public street gardens.

Location **Tests**	**1**	**2**	**3**	**4**	**5**
Electrical conductivity (EC)	0.273	0.352	0.910	0.751	0.734
pH	6.4	6.5	6.7	6.3	6.4
Total dissolved solid (TDS)	130	111	98	126	134
Total nitrogen	0.056	0.073	0.085	0.088	0.060
Phosphorus	2.963	4.5	2.1	5.3	3.7
Dissolved potassium	79.468	85.986	83.312	76.429	78.111
Sulphate	86.119	97.041	101.233	84.265	87.632
Calcium	69.680	70.871	55.936	67.453	71.519
Magnesium	21.401	23.864	15.631	19.549	24.773
organic matter	1.276	1.324	1.289	0.983	1.212
Texture	Sand loam	Sand loam	Sand loam	Sand loam	Sand loam
Clay	2	5	5	3	4
Silt	38	41	43	35	30
Sand	60	58	71	69	66

As per Abad *et al.* [23], the soil obtained from the street showed higher EC values than the soil from the dwellings, indicating a difference in EC values between the two soil types in the current investigation. The soil and the garbage were factors in the changes in the soil EC measured in this study. Garbage may be a reason for the elevated rise in the EC values of the soil. The concentrations of ions and salts in the liquid and solid phases are equal within the soil system. Therefore, the parameters controlling the sorption, solubilization, and mineralization/immobilization processes in soil significantly impact the ion concentrations determining the EC of the soil. The average pH values did not show significant changes ($p \leq 0.05$) from the sample collection sites throughout the study period. This indicates that most readings were consistent due to the same environmental conditions influencing them during sample collection. During the study period, there were significant differences ($p \leq 0.05$) in the average values of total dissolved solids compared to the sample collection sites. It indicates that street soil's total dissolved solids were higher than house soil's. The soil is primarily impacted by variations in the total dissolved solids values, which also influence the soil's qualities and attributes. The average values of the two sites showed a significant difference ($p \leq 0.05$) between them, evident from the total nitrogen values range, which recorded a massive variance in their values during the study period. The source of the irrigation water, which is primarily influenced by weather patterns, increases in ion concentrations from soil washing, and increased ion dissolution from increased rainfall, relative humidity, and soil moisture, is most likely the cause of the variation in average values between the two sites [23]. The current study's results also demonstrated notable calcium, magnesium, potassium, and Phosphorus variations at the site level. Street soil, on the other hand, has the lowest levels of these elements when compared to house soil, which is reflected in plant growth for potential Phosphorus has indirect impacts on soil because its availability influences the development of roots and branches, which enhances vegetation cover, the amount of organic matter in plants, and the outcomes of primary and secondary metabolism [24]. The current study's findings also demonstrated notable variations in sulfate levels, with house soil having the lowest sulfate content compared to soil obtained from the streets. The present study's findings also demonstrated notable variations in the amounts of organic matter, demonstrating that the group of streets' soil has the lowest quantity of organic matter compared to the soil of residences. Because the organic matter is sufficiently rich in nitrogen, it will break down and produce nitrates and ammonium nitrogen through a process known as mineralization. However, when organic matter decomposes at low nitrogen levels, nitrogen, and ammonium are consumed or immobilized because degrading microbes take available nitrogen out of the soil system, known as immobilization [25].

3.2 Vegetative growth

Table 3 shows some of the leaf measurements that were studied, and the results show a significant ($P \leq 0.05$) decrease in average leaf area in leaves collected from public street gardens (4.366 ± 0.203) compared to olive leaves collected from home gardens (4.95 ± 0.254). Leaf dry matter in leaves collected from public street gardens (39.456 ± 3.28) showed a significant ($P \leq 0.05$) decrease compared to olive leaves collected from home gardens (56.942 ± 4.87). Leaf ash also showed a significant ($P \leq 0.05$) decrease in average leaf area in leaves collected from public street gardens (8.12 ± 0.378) compared to olive leaves collected from home gardens (7.114 ± 0.137).

Table 3: shows some of the Vegetative growth measurements that were studied.

Locations Parameters	Home Gardens	Public street Gardens	P value
Average leaf area (cm^2) at harvest	4.95 ± 0.254	4.366 ± 0.203*	0.02
Leaf dry matter %	56.942 ± 4.87	39.456 ± 3.28*	0.0001
Leaf ash %	8.12 ± 0.378	7.114 ± 0.137*	0.0001

Table 4 also shows some structural characteristics of the leaf, as the vascular cylinder, cuticle layer, mesophyll, and epidermis were smaller in the leaves of the group from Home Gardens than the leaves of the Public Street Gardens group. In contrast, the leaf edge and thickness were more significant in the leaves of the group from home gardens than the leaves of public street gardens. Figure 1 shows the structure and layers of the leaf under an optical microscope.

Table 4: shows some of the leaf structures that were studied.

Locations Structures (μm)	Home gardens	Public street gardens
Vascular cylinder	330	400
Leaf thickness	500	450
Cuticle	50	100
Epidermis	10	30
Mesophyll	200	220

The current study's findings demonstrated that house soil had a more significant effect on some olive leaf characteristics than olive leaves in public street gardens, as evidenced by the superior average leaf area, dry matter, ash, edge, and thickness of olive leaves grown in home gardens. The primary cause could be the high concentration of some aspects in residential soil, such as nitrogen (N), which is an essential ingredient for crop growth and development and will inhibit plant growth if not absorbed in suitable amounts [26]. The complicated growth process is impacted by the uptake of nutrients and the availability of moisture; nitrate is crucial for absorbing and transferring to developing organs [27]. Because it provides the necessary water, the presence of this element constantly promotes growth and performance. Additionally, the terminal meristem of the stem and the lateral buds of older leaves produce more leaves when soil N is present and abundant. In the end, it raises the aerial parts' yield [28]. Conversely, sufficient phosphorus feeding improves flowering, fruiting (including seed formation), maturity, and photosynthesis. In meristematic tissues, phosphorus is essential for cell division and growth. Phosphorus promotes the development of roots, especially lateral roots and fibrous rootlets. Sufficient phosphorus supplies are necessary for adequate biological nitrogen-fixing [29].

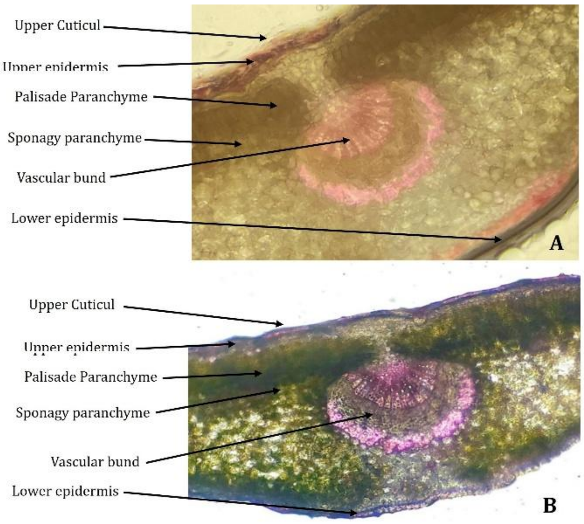

Figure 1: Cross section of olive leaves, A: Home gardens, and B: Public Street gardens.

4. Conclusions

The current study found that soil with better chemical and physical properties positively affected olive leaf growth. Among the most important elements were total nitrogen, phosphorus, and even soil organic matter, which directly affected olive leaf characteristics.

Data Availability

The datasets used and analyzed during the current study are available from the corresponding author upon reasonable request.

Conflict of Interest

The authors declare no conflict of interest.

References

[1] Mohammed, B.K., Noori, I.M. (2008) Effect of Irrigation levels on the growth and yield of olive trees (*Olea europaea* L. cv. Ashrasie), *Journal of Kirkuk University–Scientific Studies* **3**: 169-183.

[2] Faris, A.S., Abdulqader, S.M. (2024) Response of Olive Trees (*Olea europaea* L.) cv. Zaity to Bio health and Foliar Spray of Tecamin max and Boron, *Kufa Journal for Agricultural Sciences* **16**: 113-130.

[3] Salim, H.K.M., Taha, S.M. (2022) Effect of Biostimulant and Humic Acid on Tree Growth and Fruit Characteristics of Olive (*Olea europaea* L.) cv. Arbequina, *Kirkuk University Journal for Agricultural Sciences* **13**: 240-254.

[4] Rozbiany, P.M.K., Muhammad, P. (2022) Influences of humic acid and sea force on olive tree growth (*Olea europaea* L.), *Kirkuk University Journal for Agricultural Sciences* **13**: 255-263.

[5] Abd-Oun, A.K. (2019) Effect of nutrients solution spray dates on some growth characteristics of olive seedlings, *Plant Archives* **19**: 140-143.

[6] Abo-Gabien, M., Atawia, A., El-Badawy, H., El-Gioushy, S., Bakeer, S.(2020) Effect of magnetic Iron and potassium humate on some flowering and fruiting aspects of olive trees under salt stress conditions in South Sinai. 5th International Conference on Biotechnology Applications in Agriculture (ICBAA), Benha University, Egypt, pp. 8-11.

[7] Espejo-Pérez, A.J., Rodríguez-Lizana, A., Ordóñez, R., Giráldez, J.V. (2013) Soil Loss and Runoff Reduction in Olive-Tree Dry-Farming with Cover Crops, *Soil Science Society of America Journal* **77**: 2140-2148.

[8] Saeed, G.M. (2021) Effect of cultivars, date, and iba on vegetative growth of semi-hard wood olive cuttings (*Olea europaea* L.), *Journal of Duhok University* **24**: 134-142.

[9] Raza, B.M., Amin, H.M., Abdul-Razzaq, H.A.-E. (2021) The Effectiveness of Olive Oil to Combat Lice in Pregnant Women and Children, *Indian Journal of Forensic Medicine & Toxicology* **15**: 2080-2082.

[10] García-Orenes, F., Roldán, A., Mataix-Solera, J., Cerdà, A., Campoy, M., Arcenegui, V., Caravaca, F. (2012) Soil structural stability and erosion rates influenced by agricultural management practices in a semi-arid Mediterranean agro-ecosystem, *Soil Use and Management* **28**: 571-579.

[11] Lateef, M.A. (2019) Effect of foliar application by organic matter and NPK on growth and yield of olive trees, *Kirkuk University Journal for Agricultural Sciences* **10**: 36-39.

[12] Rodrigo-Comino, J., Keesstra, S., Cerdà, A. (2018) Soil Erosion as an Environmental Concern in Vineyards: The Case Study of Celler del Roure, Eastern Spain, by Means of Rainfall Simulation Experiments, *Beverages* **4**: 31.

[13] Keesstra, S.D., Rodrigo-Comino, J., Novara, A., Giménez-Morera, A., Pulido, M., Di Prima, S., Cerdà, A. (2019) Straw mulch as a sustainable solution to decrease runoff and erosion in glyphosate-treated clementine plantations in Eastern Spain. An assessment using rainfall simulation experiments, *CATENA* **174**: 95-103.

[14] Taqi, A.H., Al Nuaimy, Q.A.M., Karem, G.A. (2016) Study of the properties of soil in Kirkuk, IRAQ, *Journal of Radiation Research and Applied Sciences* **9**: 259-265.

[15] Saykhul, A., Chatzissawidis, C., Therios, I., Dimassi, K., Chatzistathis, T. (2014) Growth and nutrient status of olive plants as influenced by foliar potassium applications, *Journal of Soil Science and Plant Nutrition* **14**: 602-615.

[16] Organization, W.H. (2002) Guidelines for drinking-water quality, 2nd ed., World Health Organization, WHO, Malta, pp.

[17] Dickman, S.R., Bray, R.H. (1940) Colorimetric Determination of Phosphate, *Industrial & Engineering Chemistry Analytical Edition* **12**: 665-668.

[18] Weil, R., Brady, N. (2017) The nature and properties of soils, 15th ed., Pearson, Boston, USA, pp. 6433-6695.

[19] Rahim, S.A., Salim, A.Y., Shereef, S. (1973) Absorptiometric determination of trace amounts of sulphide ion in water, *Analyst* **98**: 851-856.

[20] Ryan, J., Estefan, G., Rashid, A. (2001) Soil and Plant Analysis Laboratory Manual, 2nd ed., International Center for Agricultural Research in the Dry Areas (ICARDA), Aleppo, Syria, pp.

[21] Helrich, K. (1975) Official Methods of Analysis, Association of Official Analytical Chemists Washington DC, USA, pp. 1230.

[22] Johansen, D. (1940) Plant Microtechnique, ed., Mc-Graw-Hillbook Company, New York, USA, pp. 523.

[23] Abad, M., Noguera, P., Burés, S. (2001) National inventory of organic wastes for use as growing media for ornamental potted plant production: case study in Spain, *Bioresource Technology* **77**: 197-200.

[24] Abdallah, A.M., Jat, H.S., Choudhary, M., Abdelaty, E.F., Sharma, P.C., Jat, M.L. (2021) Conservation Agriculture Effects on Soil Water Holding Capacity and Water-Saving Varied with Management Practices and Agroecological Conditions: A Review, *Agronomy* **11**: 1681.

[25] Facelli, J.M., Pickett, S.T.A. (1991) Plant litter: Its dynamics and effects on plant community structure, *The Botanical Review* **57**: 1-32.

[26] Cabrera, M.L., Kissel, D.E., Vigil, M.F. (2005) Nitrogen Mineralization from Organic Residues, *Journal of Environmental Quality* **34**: 75-79.

[27] Fathi, A., Farnia, A., Maleki, A. (2013) Effects of nitrogen and phosphorous biofertilizers on yield and yield components of corn AS71 in Dareh-shahr, Iran, *Journal of Crop Ecophysiology* **7**: 105–114.

[28] Fathi, A., Zeidali, E. (2021) Conservation tillage and nitrogen fertilizer: a review of corn growth and yield and weed management, *Central Asian Journal of Plant Science Innovation* **1**: 121-142.

[29] Fathi, A. (2020) Tillage systems and use of chemical fertilizers (N.P.K) Interaction on soil properties and maize quantitative and qualitative traits. *Agronomy*, Ph.D. Thesis, Faculty of Agriculture, Islamic Azad University, Ayatollah Amoli Branch, Azad.

Thamar University Journal of Natural & Applied Sciences **9**(2) (2024) 10–15

DOI: https://doi.org/10.59167/tujnas.v9i2.2310

TUJNAS

Original Article

Electrochemical synthesis of stabilizer-free silver nanoparticles with antibacterial properties

Mohammed Ahmed Hussein Awad[1],*, Yasmin M.S. Jamil[2], and Hussein M.A. Al Maydama[2]

[1]Department of Chemistry, Faculty of Applied Science, Thamar University, Dhamar 87246, Yemen.
[2]Department of Chemistry, Faculty of Science, Sana'a University, Sana'a, Yemen.

*Corresponding author: M.A.H. Awad at Department of Chemistry, Faculty of Applied Science, Thamar University, Dhamar 87246, Yemen, E-mail: mohammed.awad@tu.edu.ye

Received: 30 September 2024. Received (in revised form): 13 November 2024. Accepted: 14 November 2024. Published: 26 December 2024.

Abstract:

In this study, we present an electrochemical method for preparing silver nanoparticles (Ag NPs) powder using a metallic silver cathode and anode in an aqueous solution of doubled distilled water (DW) with a voltage of about 27 volts. The method does not involve the use of any chemical stabilizing agents. The synthesized Ag nanoparticles were characterized using X-ray diffraction (XRD) analysis and UV-visible Spectroscopy (UV). The experiment results indicate that the crystal structure of the Ag nanoparticles sample is face-centered cubic (FCC) structure the same as the bulk materials, the crystalline size distribution ranging from 15.86 to 21.30 nm, with an average crystalline size of about 18.7 nm obtained by XRD results. Colloidal silver-NPs with a grain size of 18.7 nm were produced at optimum conditions. A peak at 406 nm was obtained in UV-visible spectroscopy attributed to Ag NPs. In addition, the synthesized Ag nanoparticles revealed a tremendous antibacterial effect against pathogenic microorganisms.

Keywords: Electrochemical Preparation; Ag Nanoparticles; XRD analysis; UV-vis spectroscopy; Antimicrobial activity.

1. Introduction

The study of silver nanoparticles has been of great scientific interest due to their physical and chemical properties, their characteristics differ depending on their size or shape. The study of Ag nanoparticles (Ag NPs) has taken various applications in medicine, catalysis, biotechnology, bioengineering, optics, and antibacterials in water treatment [1–3]. The optical properties of Ag NPs depend on their size. So many efforts are being made to synthesize Ag NPs, which are very important [4]. The effectiveness of Ag NPs as antimicrobials and antibacterials has been determined, particularly in medicine and water treatment. Antibacterial activity has been analyzed in *Streptococcus mutans*, *Staphylococcus aureus*, and *Escherichia coli*; as a result, the nanoparticles release silver ions in the bacterial cells, causing cell death of the bacteria or microbe [5–7].

For the synthesis of Ag-NP, there are several chemical and physical methods; in the chemical method, the synthesis of Ag-NP is carried out by the chemical reduction of silver salts under a reducing agent [8, 9], as that prepared by chemical reduction method using PVP (Polyvinyl pyrrolidone) [10]. In the search for environmentally friendly methods, a good option is the synthesis of Ag NPs by electrochemical reduction. The electrochemical method consists of obtaining Ag NPs formed from the reduction of a silver cathode; a main advantage of the electrochemical method is the purity of the silver particles and the possibility to control the concentration and size of the Ag NPs by varying the temperature and current density. The electrochemical method presents a limitation since the deposit of silver on the cathode during the process decreases the effective surface to produce particles. At a certain time, the production of particles ceases. Inverting the polarity at a certain time generates an anode-cathode variation with a constant voltage and avoids the deposit of silver on the cathode to obtain higher concentrations. Thus, Ag nanoparticles were synthesized in this work by reversing polarity every 60 seconds, obtaining Ag nanoparticles. The problems that the researchers in Ag NP synthesis are the complex methods of Ag NP synthesis by high prices and using more chemicals.

This search aims to prepare Ag NP powder using a fast, low-cost, and environmentally friendly electrochemical method. By applying appropriate conditions, small size, high purity, and high quantity of Ag NPs can be obtained. The Ag nanoparticles were characterized by XRD [11–15] and UV-visible Spectroscopy. The antimicrobial activity of Ag NPs was tested.

2. Experimental

2.1. Materials

Table 1: Chemicals and materials used.

Sequences	Raw materials
1	Silver electrodes with high purity reach 99.99% in dimensions (1 mm x 20 mm x 50 mm).
2	Double distilled deionized water (DW).
3	Mueller-Hinton agar (MHA, HIMEDIA, India)

2.2. Synthesis of Ag nanoparticles

The characterizations of the electrochemical method for producing nanoparticles can be described by high-purity particles and the possibility of controlling the size of the nanoparticles by controlling the current density. This method is easy and effective for producing nanoparticles without chemicals and maintains stability.

This method includes using two electrodes, anode and cathode plates made of silver with high purity, reaching 99.99%, and with dimensions (1 mm x 20 mm x 50 mm). The two electrodes are placed facing each other in a vertical way with a distance of 10 mm between each other; the set-up is placed into the electrical cell that contains 500 ml double distilled deionized water (DW). The silver particles precipitate on the cathode during the electrolysis. The electrolysis has been employed at room temperature (293 K) with continuous voltage (27.0 V), and the current passed in the circuit has been monitored with a voltmeter. Additionally, the electrical circuit has been controlled to change the Polarity between the electrodes according to the optimal period of 4 minutes. The production of nanoparticles in an electrochemical reduction manner involves changing the polarity of the direct current between the poles in addition to steering during the electrolysis process to prevent precipitation. Figure 1 shows the process of formation of colloidal silver nanoparticles in the electrochemical method as follows:

1) The oxidation of silver at the anode as shown below:

$$Ag^0 - e^- \rightarrow Ag^+ \qquad (1)$$

2) The release of oxygen gas due to the electrolysis of water:

$$2H_2O - 4e^- \rightarrow O_2\uparrow + 4H^+ \qquad (2)$$

At the same time, the deposition layer of Ag_2O is on the surface of the anode.

3) Immigration of the silver ions to the cathode.
4) Reduction of the ions and formation of the silver atoms on the cathode:

$$Ag^+ + e^- \rightarrow Ag^0 \qquad (3)$$

The releasing of hydrogen gas during the process:

$$2H_2O + 2e^- \rightarrow H_2 + 2OH^- \qquad (4)$$

5) Formation of the silver particles via the nucleation and the growth due to Van der Waals attraction.
6) Separation of the silver nanoparticles formed due to the severe steering.

In this process, the regular exchange of D.C current polarity may reduce the silver deposition rate on the cathode. During the exchange of polarity, the formed on the anode before will be hydrated during the interaction with the hydrogen gas:

$$Ag_2O + H_2 \rightarrow 2Ag + H_2O \qquad (5)$$

The duration used for exchanging the polarity was 4 min. Below this time, particles would accumulate due to the gradual reduction of the surface pole's efficiency [16].

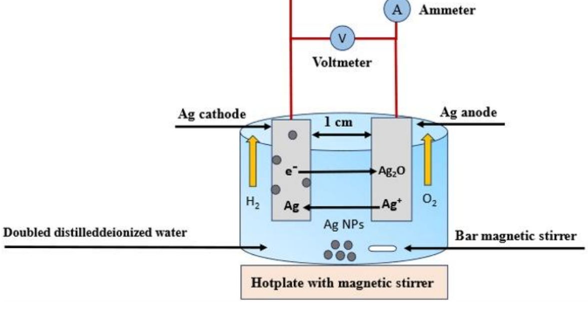

Figure 1: Illustrates the scheme of the formation of silver nanoparticles using the electrochemical method.

2.3. Physicochemical Measurements

The Ag nanoparticles were characterized by XRD (XD-2 X-ray Diffractometer) with Cu-Kα radiation (λ = 0.15418 nm; 40 kV and 40 mA). The intensity was 0-2500 counts per second (cps), and the 2 (deg) scope was 5-76 degrees. The UV-vis absorption spectrum of the prepared Ag NPs is measured using (50 conc) spectrophotometer, covering a range from (200-800) nm.

2.4. Antimicrobial activity of Ag nanoparticles

The antibacterial activity of silver nanoparticles was discovered using a well diffusion method [17,18]. Gram-negative bacteria (-) like *Pseudomonas (P.S), Escherichia coli Salmonella (S), Klebsiella (K)* and Gram-positive bacteria (+) like *Strep pyogenes (S.P)* and *Staphylococcus aureus (S.U)* were employed as microorganism strains for the antibacterial research. Sterile wells measuring 6 mm in diameter were welled on swabbed MHA plates. Various concentrations of Ag nanoparticles (100, 200, 400, and 500 mg/mL) were poured over the wells (70 μL). The negative control was sterile distilled water, and the positive control was amoxicillin. For 24 h, at 37 °C, the plates were cultured. An inhibitory zone is also detected in mm after the incubation.

3. Results and Discussion

3.1. XRD analysis

3.1.1 Structural analysis

Figure 2 shows the typical X-ray diffraction pattern for the specimen. The broad diffraction peaks suggest that the sample consists of very small particles. The major peaks of the pure Ag powders are observed. Three broad peaks with 2θ values of 38.1º, 44.4º, and 64.6º correspond to the (111), (200), and (220) planes of the bulk Ag, respectively, which can be assigned to the Ag FCC structure. The XRD pattern shows that the samples are single phase, and no other distinct diffraction peak, except the characteristic peaks of FCC phase Ag, was found [19].

From the full width at half maximum, the crystallite size for the sample can be calculated from the XRD peaks according to Scherrer formula [20-22]:

$$D_{\text{crystallite}} = \frac{K\lambda}{\beta \cos\theta} \qquad (6)$$

Where $D_{\text{crystallite}}$ is the crystallite size, K = 0.89 is the Scherrer constant related to the shape and index (hkl) of the crystals, λ is the wavelength of the X-ray (Cu Ka, 1.54056 Aº), θ is the diffraction angle, and β is the corrected full width at half maximum (FWHM) (in radian). The average crystallite size (grain size) was about 18.7 nm (see Table 2).

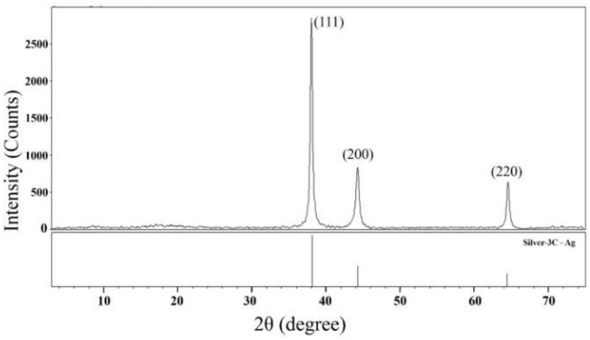

Figure 2: XRD pattern of Ag nanoparticles.

The lattice parameters (a, b, and c) for Ag nanoparticles with a face-centered cubic (FCC) crystal structure were calculated as in Table 3. The lattice parameters (a, b, and c) (Table 2) are almost identical to those reported in the (JCPDS 04-0783) card for Ag [23,24]. The d-spacing values obtained from the Braggs' law (7) and the theoretical (8) equations [25] were almost identical, as can be seen in Table 3.

$$n \times \lambda = 2d \times \sin(\theta) \Leftrightarrow d = \frac{n\lambda}{2\sin\theta} \qquad (7)$$

$$1/d^2 = [(h^2 + k^2 + l^2) / a^2] \Leftrightarrow d_{hkl} = a / \sqrt{(h^2 + k^2 + l^2)} \qquad (8)$$

Table 2: Crystallite size calculations of Ag nanoparticles using Scherrer's equation.

Plane (*hkl*)	(2θ)°	(θ)°	θ (rad)	cos (θ) (rad)	*β*°	*β* (rad)	D_{hkl} (nm)	D_{ave} (nm)
111	38.1	19.05	0.3324852	0.9999832	0.373	0.0065101	21.30	**18.7**
200	44.4	22.2	0.3874631	0.9999771	0.501	0.0087441	15.86	
220	64.6	32.3	0.5637413	0.9999516	0.420	0.0073304	18.92	

Table 3: Ag nanoparticles lattice parameters (a, b, and c) and the inter-planer d-spacing.

Plane (*hkl*)	2θ°	Lattice parameters (Å)		Average Volume (V = a³) (Å³)	d (Å) Practical	d (Å) theoretical
		A = b = c (FCC)	average			
111	38.1	4.0856	4.0794	67.8859	2.3588	2.3588
200	44.4	4.0776			2.0388	2.0388
220	64.6	4.0749			1.4407	1.4407

3.1.2 Specific surface area (SSA)

The surface area plays a critical role inside the nanoparticles due to their large surface-to-size ratio with a lower crystallite size [26]. SSA is a material property. It is a systematic value that can be used to determine a material's nature and qualities. In the context of adsorption, heterogeneous catalysis, and surface reactions, it is particularly significant. SSA stands for each mass's surface area (SA). According to Zhang's report [27], as material sizes shrink, the precise surface area and surface-to-volume ratio drastically increase. Mathematically, SSA can be computed using the following formula [28], and the calculated data are shown in Table 4.

$$SSA = 6 \times 10^3/D\,\rho \qquad (9)$$

where SSA is the specific surface area, D is the crystallite size, and ρ is the density of nanoparticles ($\rho(Ag)=10.491$ g cm^{-3}) [29]. Table 4 shows that the average SSA for Ag nanoparticles is 31.05 m^2 /g.

3.1.3 Dislocation density

A material's unit lattice, an atom or an ion, has a liner flaw called a dislocation. The disordering of these units in an array by some mechanisms, such as the absence of atoms or the existence of impurities, results in their dislocation. For some of the material's properties, like its mechanical and electrical properties, this flaw may be more advantageous. Industrially, these changes in lattice structure may be desired according to the resultant properties. The crystallinity of the substance is related to this lattice deformation [30].

The crystallite size and dislocation density can be computed using X-ray line profile analysis [31]. Owing to the importance of the dislocation density (δ) in the mechanical and structural properties of materials [32], it was calculated for the prepared Ag nanoparticles. The dislocation density (δ) in the sample was calculated using the expression $\delta = 1/D^2$, and the results are shown in Table 4. The δ average of Ag nanoparticles is 2.991× 10^{15} m^{-2}.

3.1.4 Morphology index (MI)

It is well known that the peak broadening in the XRD pattern is due to the finite size of the particles. The width of the diffraction peaks increases with the decrease in crystallite size. The morphology index (MI) is used to affirm the uniformity and fineness of the prepared nanoparticles. It is calculated using the full width half maximum (FWHM) of the XRD peak. MI indicates that the specific surface area of Ag nanoparticles relies on the interrelationships between particle morphology and size. MI is calculated as follows: $MI = FWHM_h/(FWHM_h + FWHM_p)$ [33], where $FWHM_h$ is the highest value of full width half maximum of XRD peaks, and $FWHM_p$ is the specific value of full width half maximum of a peak where the MI has to be computed. These results are plotted in Figures 3 and 4.

The details are shown in Table 4. The MI range of Ag nanoparticles is from 0.50 to 0.573. It is discovered that MI is, with a minor variation, directly proportional to crystallite size and inversely proportional to exact surface area. The deviations and relationships between them are indicated by the linear ft within the figure. The uniformity and fitness of the prepared nanoparticles are confirmed by the MI results. Figure 5 shows that the SSA of Ag nanoparticles is inversely proportional to the crystallite size.

Table 4: Morphology Index, specific surface area, and dislocation density of Ag nanoparticles.

Plane (hkl)	2θ°	Scherrer D (nm)	Specific Surface Area (SSA) (m²/g)	Morphology Index (MI) (unitless)	Dislocation Density (δ) (m⁻²) × 10¹⁵	Average (δ) (m⁻²)
111	38.1	21.30	26.85	0.573	2.204	2.991× 10¹⁵
200	44.4	15.86	36.06	0.50	3.976	
220	64.6	18.92	30.23	0.544	2.794	

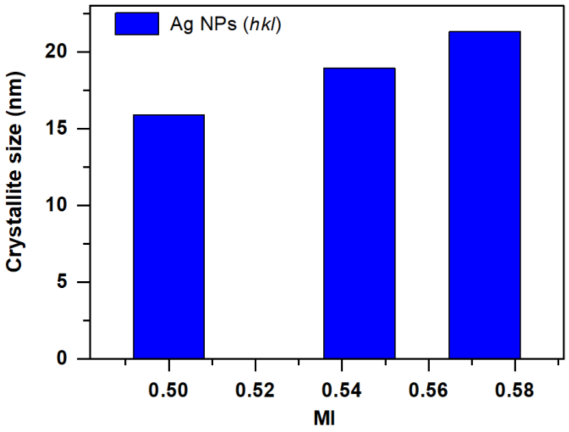

Figure 3: Morphological index vs crystallite size of Ag nanoparticles.

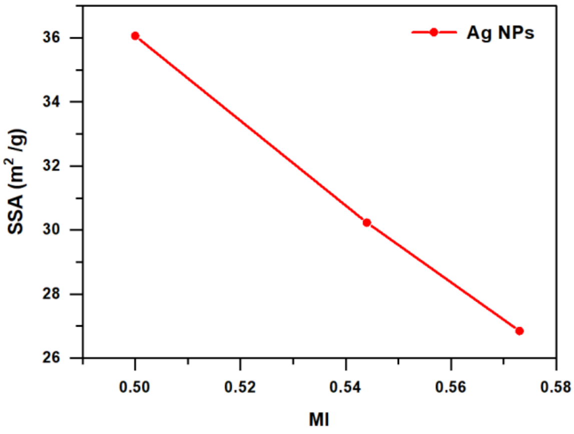

Figure 4: MI Vs specific surface area of an Ag nanoparticles (hkl).

3.2. UV-Visible spectroscopy

Plasmon bands are inimitable physical properties of nanoparticles. The surface plasmon resonance (SPR) is mostly determined by means of the dielectric properties of the metal and the surrounding medium, over and above the particle size and shape. The position of plasmon absorption bands of metallic NPs depended on the size and shape of nanostructures [34].

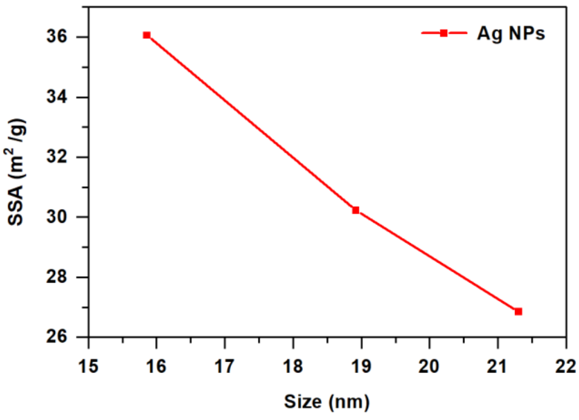

Figure 5: Size vs Specific Surface Area of Ag nanoparticles.

The optical properties of the Ag nanoparticles were investigated using the UV-VIS technique. It is well known that colloidal silver nanoparticles exhibit a broad absorption band at the wavelength from 390 to 420 nm due to Mie scattering [35,36]. The maximum absorbance observed at 406 nm is the characteristic peak of silver nanoparticle material, attributed to the localized surface plasmon resonance (LSPR) of Ag NPs [37], as shown in Figure 6. UV–VIS absorption results confirmed the formation of silver nanoparticles prepared by the electrochemical method.

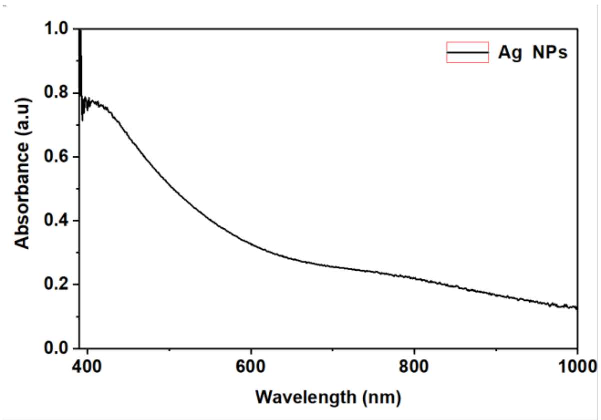

Figure 6: UV-visible spectrum of Ag NPs as a function of wavelength.

3.3. Antibacterial Activity

3.3.1 The antibacterial effect of Ag nanoparticles

Figure 7 shows the antimicrobial activity of Ag nanoparticles with concentrations (100, 200, 400, and 500 mg/mL) against *Pseudomonas (P. S)*, *Streptopyogens (S. P)*, *Escherichia coli (E. coli)*, *Salmonella (S)*, *Klebsiella (K)* and *Staphylococcus aureus (S. aureus – S.U)* bacteria (Figure 8). Synthesized nanoparticles by electrochemical methods have been found to be highly toxic against pathogenic bacteria. The antibacterial activity of silver nanoparticles can be modified with the size of silver nanoparticles, where it decreases with an increase in the particle size [38].

Table 5: Ag nanoparticles concentrations (mg/mL) and inhibition diameter (mm) of bacteria strains, the symbol (+) refers to gram-positive bacteria while the symbol (-) refers to gram-negative bacteria.

Ag NPs concentration in (mg/mL)	Inhibition zone of bacteria in (mm)					
	P.S (-)	*S.P* (+)	*E. coli* (-)	*S* (-)	*K* (-)	*S.U* (+)
100	36	30	16	26	16	16
200	38	25	15	26	14	21
400	36	28	25	34	16	26
500	38	27	17	38	15	25

After 24 hrs. of incubation, the zone of inhibition was calculated in all plates (width in mm). For six distinctive bacterial strains, gram-positive bacteria (+) and gram-negative bacteria (-), the development sector of inhibition (Table 5) was detected for some distinct concentrations of synthesized silver nanoparticles. The power of Ag NPs against the tested bacteria depended on the size and dose. The zone of inhibition in some bacteria strains increases with the increasing dose of silver nanoparticles [39]. The Ag NPs showed excellent antibacterial activity against all tested isolates, particularly against *Pseudomonas (P.S)* and Salmonella *(S)* as shown in Table 5 and Figure 8.

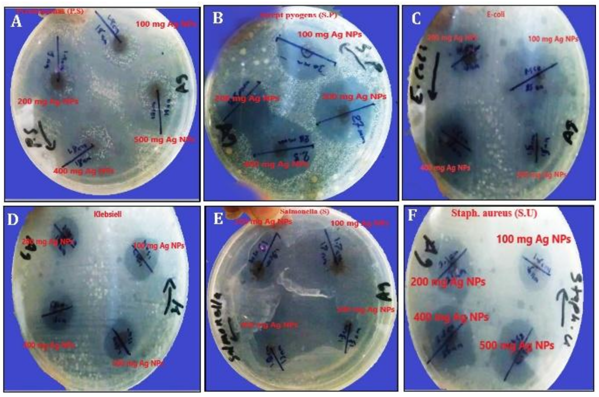

Figure 7: Antibacterial assay: zone of inhibition of Ag nanoparticles against the tested bacterial strains: (A) *Pseudomonas (P. S)*, (B) *Streptopyogens (S. P)*, (C) *Escherichia coli (E. coli)*, (D) *Klebsiella (K)*, (E) *Salmonella (S)*, and (F) *Staphylococcus aureus (S. aureus – S.U)*.

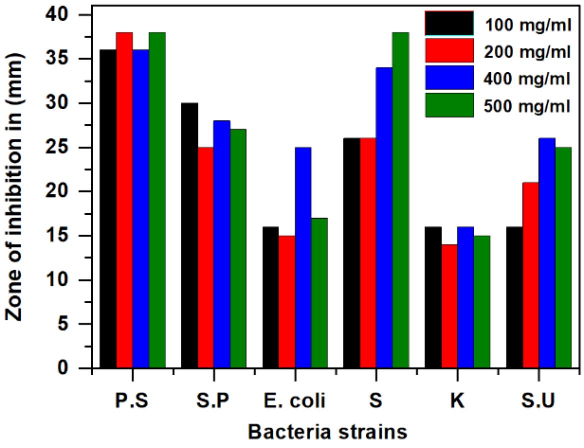

Figure 8: Comparative representation of zone of inhibition of Ag nanoparticles in diameters formed against the tested bacterial strains.

From Table 5, the antibacterial effectiveness of Ag NPs showed that *Pseudomonas (P.S)* recorded the most significant susceptibility, with inhibitory zones rising from 36 mm to 38 mm as the Ag NPs increased from 100 mg/mL to 500 mg/mL. Ag NPs' impact on *Streptpyogens (S.P)* depended on the concentration used. An inhibitory zone of 30 mm was observed at 100 mg/mL. At greater dosages of 200, 400, and 500 mg/mL, inhibitory zones measuring 25 mm, 28 mm, and 27 mm were found. The reduced inhibition at a concentration of 500 mg/mL indicates potential for nanoparticle aggregation, decreasing the surface area accessible for antibacterial action [40]. *E-coli* bacteria showed larger inhibitory zones at greater concentrations of Ag NPs. Specifically, at 400 and 500 mg/mL dosages, the zones measured 25 mm and 17 mm, respectively. The 100 and 200 mg/mL inhibition zones were 16 and 15 mm, respectively. The minor decrease in zone size as the concentration increases may be due to possible aggregation effects [40]. Concerning *Salmonella (S)* bacteria, the zone of inhibition increases with the increasing dose of silver nanoparticles. The inhibition zones of 100, 200, 400, and 500 mg/mL dosages were 26, 26, 34, and 38 mm, respectively. *Klebsiella (K)* bacteria showed the inhibition zone at 100, 200, 400, and 500 mg/mL dosages, measuring 16, 14,16, and 15 mm, respectively. A modest decrease in activity (15 mm inhibitory zone) was observed at the highest dose of 500 mg/mL, possibly due to nanoparticle aggregation reducing their effective surface area [40]. Concerning *Staph. Aureus (S.U)* bacteria, the zone of the inhibition increases with the increasing dose of silver nanoparticles. The inhibition zones of

100, 200, 400, and 500 mg/mL dosages were 16, 21, 26, and 25 mm, respectively. Ag NPs had different impacts on *Staph. Aureus (S.U) bacteria*, resulting in zone sizes of 16 mm (100 mg/mL), 21 mm (200 mg/mL), a notable increase to 26 mm (400 mg/mL), and then a decrease to 25 mm (500 mg/mL). Based on these findings, an ideal antibacterial dosage of around 400 mg/mL is recommended for combating *Staph. Aureus (S.U)* bacteria. The differences in antibacterial effectiveness shown in various bacteria may be due to variations in cell wall composition [40]. It is reported that the Ag nanoparticles with an average particle size range between 30 nm and 35 nm exhibit antibacterial activity more than some antibiotics like Ciprofloxacin 5, Vancomycin 30, and Ampicillin 10 [18]. Also, it is stated that the zone of inhibition in mm for 8 ppm concentration of Ag nanoparticles prepared by electrochemical method, with particle size between 30-70 nm, was 12 mm against *E-coli* bacteria [41]. The zone of inhibition for 100 $\frac{\mu g}{ml}$ *of* Ag NPs (average particle size between 20 to 45 nm) against *Pseudomonas* bacteria was 5 mm, and for Amoxicillin antibiotic was between 8-10 mm [42]. The zone of inhibition for 50 μg *of* Ag NPs (average particle size 29 nm) against *E. coli* bacteria was 13 mm, for *Staphylococcus aureus*, 12 mm, and for *Pseudomonas* bacteria, 17 nm, whereas for 10 µg tetracycline antibiotic, they were 10-11 mm [39].

Ag nanoparticles have inhibitive activity against tested bacteria strains because of small size of nanoparticles and their large surface area that is to say when the size of nanoparticles is small, the nanoparticles congregate on the cell surfaces and that result in increasing in their toxicity against microorganisms and that will affect on permeability of plasma membrane and result in cell death [43].

3.3.2 Antibacterial Mechanism of Silver Nanoparticles

Even though the precise mechanism of silver nanoparticles' antibacterial effects has not been completely elucidated, several antibacterial actions have been suggested. The probable antimicrobial mechanisms suggested comprise (1) Disruption of the cell wall and cytoplasmic membrane: silver ions (Ag^+) released by silver nanoparticles adhere to or pass through the cell wall and cytoplasmic membrane. (2) Denaturation of ribosomes: silver ions denature ribosomes and prohibit protein synthesis. (3) Interruption of adenosine triphosphate (ATP) production: ATP production is terminated for the purpose that silver ions deactivate respiratory enzymes on the cytoplasmic membrane. (4) Membrane disruption via reactive oxygen species (ROS): reactive oxygen species generated via the broken electron transport chain can cause membrane disruption. (5) Interference of deoxyribonucleic acid (DNA) replication: silver and reactive oxygen species bind to deoxyribonucleic acid and prevent its replication and cell multiplication. (6) Denaturation of membrane: silver nanoparticles accumulate in the pits of the cell wall and cause membrane denaturation. (7) Perforation of membrane: silver nanoparticles proceed straight across the cytoplasmic membrane, which can release organelles from the cells [44].

4. Conclusion

In brief, silver nanoparticles were successfully prepared using the electrochemical method at room temperature. The crystalline structure of the particles, confirmed by XRD, is FCC structure the same as that of the bulk materials; the crystallite size ranges from 15.86 nm to 21.30 nm with an average crystallite size of about 18.7 nm. The specific surface area average and dislocation density average of Ag nanoparticles are 31.05 m^2/g and $2.991\times 10^{15}\ m^{-2}$, respectively. The MI range of Ag nanoparticles is from 0.50 to 0.573. The characteristic peak in the UV-vis spectrum confirms the formation of Ag nanoparticles. Ag nanoparticles exhibited notably strong antimicrobial activity against clinical pathogenic bacteria like *Pseudomonas, Streptopyogens, Escherichia coli, Salmonella, Klebsiella,* and *Staphylococcus aureus.* Our outlook for the future of this research is to prepare Ag NPs using the electrochemical method to obtain different sizes of Ag NPs by controlling voltage and temperature.

Data Availability

The datasets used and analyzed during the current study are available from the corresponding author upon reasonable request.

Conflict of Interest

The authors declare no conflict of interest

References

[1] Ravindran, A., Chandran, P., & Khan, S. S. (2013) Biofunctionalized silver nanoparticles: Advances and prospects. *Colloids and Surfaces B: Bio interfaces* **105**: 342–352.

[2] Qassim Raheem, H., F. Hussein, E., Hameed Rasheed, A., & K. Imran, N. (2022) Antibacterial action of Silver Nanoparticles against Staphylococcus aureus Isolated from wound infection. *Research Journal of Pharmacy and Technology* **15**: 2413–2416.

[3] Khan, I., Saeed, K., & Khan, I. (2019) Nanoparticles: Properties, applications and toxicities. *Arabian Journal of Chemistry* **12**: 908–931.

[4] Tri Handoko, Chanel., Huda, Adri., and Gulo, Fakhili. (2019) Synthesis Pathway and Powerful Antimicrobial Properties of Silver Nanoparticle: A Critical Review. *Asian Journal of Scientific Research* **12**: 1-17.

[5] Liu, W.-T. (2006) Nanoparticles and their biological and environmental applications. *Journal of Bioscience and Bioengineering* **102**(1): 1–7.

[6] Rai, M., Yadav, A., & Gade, A. (2009) Silver nanoparticles as a new generation of antimicrobials. *Biotechnology Advances* **27**: 76–83.

[7] Bruna, T., Maldonado-Bravo, F., Jara, P., & Caro, N. (2021) Silver Nanoparticles and Their Antibacterial Applications. *International Journal of Molecular Sciences* **22**: 7202.

[8] Khan, Z., Al-Thabaiti, S.A., Obaid, A.Y., & Al-Youbi A.O. (2011) Preparation and characterization of silver nanoparticles by chemical reduction method. *Colloids and Surfaces B: Biointerfaces* **82**: 513–517.

[9] Vega-Baudrit, J., Gamboa, S.M., Rojas, E.R., & Martinez, V.V. (2019) Synthesis and characterization of silver nanoparticles and their application as an antibacterial agent. *International Journal of Biosensors & Bioelectronics* **5**: 166–173.

[10] Wang, H., Qiao, X., Chen, J., Wang, X., & Ding, S. (2005) Mechanisms of PVP in the preparation of silver nanoparticles. *Materials Chemistry and Physics* **94**: 449–453.

[11] Khaydarov, R.A., Khaydarov, R.R., Gapurova, O., Estrin, Y., & Scheper, T. (2008) Electrochemical method for the synthesis of silver nanoparticles. *Journal of Nanoparticle Research* **11**: 1193–1200.

[12] Rodríguez-Sánchez, L., Blanco, M.C., & López-Quintela, M.A. (2000) Electrochemical Synthesis of Silver Nanoparticles. *The Journal of Physical Chemistry B* **104**: 9683–9688.

[13] Darroudi, M., Ahmad, M.B., Abdullah, A.H., Ibrahim, N.A., & Shameli, K. (2010) Effect of Accelerator in Green Synthesis of Silver Nanoparticles. *International Journal of Molecular Sciences* **11**: 3898–3905.

[14] Saion, E., & Gharibshahi, E. (2014) On the theory of metal nanoparticles based on quantum mechanical calculation. *Malaysian Journal of Fundamental and Applied Sciences* **7**: 6 – 11.

[15] Jaimez Layna, G., Mejía García, C., Díaz Valdés, E., Guillén Cervantes, Á., Rojas Morales, M. de L., Avendaño Ibarra, M., Bautista Ramírez, M.E., & Lozano Rojas, K.J. (2024) Synthesis and characterization of silver nanoparticles by electrochemical method. *Materials Express* **14**: 1072–1077.

[16] Haider, M. J., & Mahdi, M. S. (2015) Synthesis of Silver Nanoparticles by Electrochemical Method. *Engineering and Technology Journal* **33**: 1361–1373.

[17] Arsene, M.M.J., Viktorovna, P.I., Alla, M., Mariya, M., Davares, A.K.L., Carime, B.Z., Anatolievna, G.O., Vyacheslavovna, Y.N., Vladimirovna, Z.A., Andreevna, S.L., Aleksandrovna, V.E., Alekseevich, B.L., Nikolaïevna, B.M., Parfait, K., and Andrey, V. (2023) Antimicrobial activity of Phyto fabricated silver nanoparticles using Carica papaya L. against Gram-negative bacteria. *Veterinary World* **16**: 13011311.

[18] Taqveem, H., Ur Rahman, K., Khan, S., Khan, A., Al-Ansi, W., Fahad, S., Nawaz, N., Karishma, N., Hussain, W., & Khan, L. A. (2024) Antibacterial Activity of Silver Nanoparticles Synthesized from Aloe Vera Extract. *International Journal of Environment Agriculture and Biotechnology* **9**: 54 – 61.

[19] Zhou, M., Wei, Z., Qiao, H., Zhu, L., Yang, H., & T. Xia. (2009) Particle Size and Pore Structure Characterization of Silver Nanoparticles Prepared by Confined Arc Plasma. *Journal of Nanomaterials* **2009**: 1 – 5.

[20] Jamil, Y. M. S., Awad, M. A. H., Al-Maydama, H. M. A., EL-Ghoul, Y., & Al-Hakimi, A. N. (2022) Synthesis and study of enhanced electrochemical properties of NiO nanoparticles deposited on TiO_2 nanotubes. *Applied Organometallic Chemistry* **36**: 1 – 15.

[21] Jamil, Y. M. S., Awad, M. A. H., Al-Maydama, H. M. A. (2022) Physicochemical Properties and Antibacterial Activity of Pt Nanoparticles on TiO_2 Nanotubes as Electrocatalyst for Methanol Oxidation Reaction. *Results in Chemistry* 4: 100531.

[22] Jamil, Y. M. S., Awad, M. A. H., Al-Maydama, H. M. A., Alhakimi, A.N., Shakdofa, M.M.E., & Mohammed, S.O. (2022) Gold nanoparticles loaded on TiO_2 nanoparticles doped with N_2 as an efficient electrocatalyst for

glucose oxidation: preparation, characterization, and electrocatalytic properties. *Journal of Analytical Science and Technology* **13**: 54.

[23] Pavani, K.V., Kumar, N.S., & Sangameswaran, B.B. (2012) Synthesis of Lead Nanoparticles by Aspergillus Species. *Polish Journal of Microbiology* **61**: 61–63.

[24] Gopinath, V., & Velusamy, P. (2013) Extracellular biosynthesis of silver nanoparticles using Bacillus sp. GP-23 and evaluation of their antifungal activity towards Fusarium oxysporum. *Spectrochimica Acta Part A: Molecular and Biomolecular Spectroscopy* **106**: 170–174.

[25] Shahjahan, M., Hasibur Rahman, Md., Hossain, M. S., Khatun, M. A., Islam A., & Begum, M. H. A. (2017) Synthesis and Characterization of Silver Nanoparticles by Sol-Gel Technique. *Nanoscience and Nanometrology* **3**: 34 – 39.

[26] Jiang, C., Wei, M., Qi, Z., Kudo, T., Honma, I., & Zhou, H. (2007) Particle size dependence of the lithium storage capability and high-rate performance of nanocrystalline anatase TiO_2 electrode. *Journal of Power Sources* **166**: 239–243.

[27] Gao, L., & Zhang, Q. (2001) Effects of amorphous contents and particle size on the photocatalytic properties of TiO_2 nanoparticles. *Scripta Materialia* **44**: 1195–1198.

[28] Pan, X., & Xu, Y.-J. (2013) Fast and spontaneous reduction of gold ions over oxygen-vacancy-rich TiO_2: A novel strategy to design defect-based composite photocatalyst. *Applied Catalysis A: General* **459**: 34–40.

[29] Aldayel, M.F., El Semary, N., & Adams, D.G. (2023) Differential Antimicrobial Effect of Three-Sized Biogenic Silver Nanoparticles as Broad-Spectrum Antibacterial Agents against Plant Pathogens. *Antibiotics* **12**: 1114.

[30] Jamil, S., & Fasehullah, M. (2021) Effect of Temperature on Structure, Morphology, and Optical Properties of TiO_2 Nanoparticles. *Materials Innovations* **1**: 22–28.

[31] Ungár, T., Tichy, G., Gubicza, J., & Hellmig, R.J. (2005) Correlation between subgrains and coherently scattering domains. *Powder Diffraction* **20**: 366–375.

[32] Ahmed, Abdullah A. A.., Al-Mushki, Asma. A.A., Al-Asbahi, Bandar. Ali., Abdulwahab, A. M., Abduljalil, Jameel. M.A., Saad, Fuad. A.A., Qaid, Saif. M.H. (2021) Effect of ethylene glycol concentration on the structural and optical properties of multimetal oxide $CdO–NiO–Fe_2O_3$ nanocomposites for antibacterial activity. *Journal of Physics and Chemistry of Solids* **155**: 110113.

[33] Othman, S.A. (2023) Characterization of Doped Titanium Dioxide (TiO_2) at Different Calcination Temperature Using X-Ray Diffraction (XRD). *ASM Science Journal* **18**: 1–8.

[34] Ahmed, Abdullah A. A., Aldeen, Thana. S., Al-Aqil, Samar. A., Alaizeri, ZabnAllah. M., and Megahed, Saad. (2022) Synthesis of Trimetallic (Ni-Cu)@Ag Core@Shell Nanoparticles without Stabilizing Materials for Antibacterial Applications. ACS Omega **7**: 37340–37350.

[35] Singh, K., Panghal, M., Kadyan, S., Chaudhary, U., & Yadav, J.P. (2014) Antibacterial Activity of Synthesized Silver Nanoparticles from *Tinosporacordifolia* against Multi Drug Resistant Strains of *Pseudomonas aeruginosa* Isolated from Burn Patients. *Journal of Nanomedicine and Nanotechnology* **5**: 192.

[36] Albashir, Mohammed. Hashim., & Mohammed, Ali. K. (2024) Influence of Stirring Time on the Electrochemical Synthesis of Silver Nanoparticles: Size and Stability Analysis. *International Journal of Research Publication and Reviews* **5**: 10065–10070.

[37] Kalainila, P., Subha, V., Ernest Ravindran, R.S., & Renganathan, Sahadevan. (2014) Synthesis and Characterization of Silver Nanoparticle from Erythrina indica. *Asian Journal of Pharmaceutical and Clinical Research* **7**: 39-43.

[38] Duque-Aristizábal, J.C., Isaza-Areiza, L.M., Tobón-Calle, D., & Londoño, M.E. (2019) Antibacterial activity of silver nanoparticles immobilized in zinc oxide-eugenol cement against Enterococcus faecalis: An in vitro study. *Revista Facultad de Odontología Universidad de Antioquia* **30**: 154–165.

[39] Nahar, Kamrun, Hafezur Rahaman, Md., Arifuzzaman Khan, G.M., Khairul Islam, Md., & Al-Reza, Sharif. M.d. (2021) Green synthesis of silver nanoparticles from *Citrus sinensis* peel extract and its antibacterial potential. *Asian Journal of Green Chemistry* **5**: 135–150.

[40] Bruna, Tamara., Maldonado-Bravo, Francisca., Jara, Paul., & Caro, Nelson. (2021) Silver Nanoparticles and Their Antibacterial Applications. *International Journal of Molecular Sciences* **22**: 7202.

[41] Sharma, Sumit., Choudhary, Kapil., Singhal, Ishu., & Saini, Rishabh. (2014) Synthesis of Silver Nanoparticles by 'Electrochemical Route' through pure metallic silver electrodes, and evaluation of their Antimicrobial Activities. *International Journal of Pharmaceutical Sciences Review and Research* **28**: 272–277.

[42] Preethi, A. Cathirin., & Krishnan, V. Harihara. (2023) The optical and electrochemical characteristics of silver nanoparticles, besides antibacterial and antifungal properties using Crocus sativus. L petals. *Research Square*, PREPRINT (Version 1) https://doi.org/10.21203/rs.3.rs-3347270/v1

[43] Lin, X., Li, J., Ma, S., Liu, G., Yang, K., Tong, M., & Lin, D. (2014) Toxicity of TiO_2 Nanoparticles to Escherichia coli: Effects of Particle Size, Crystal Phase and Water Chemistry. *PLoS ONE* **9**: e110247.

[44] Yin, Iris. Xiaoxue., Zhang, Jing., Zhao, Irene. Shuping., Mei, May. Lei., Li, Quanli., Chu, Chun. Hung. (2020) The Antibacterial Mechanism of Silver Nanoparticles and Its Application in Dentistry. *International Journal of Nanomedicine* **15**: 2555–2562.

Thamar University Journal of Natural & Applied Sciences ***9***(2) (2024) 16–22

DOI: https://doi.org/10.59167/tujnas.v9i2.2311

TUJNAS

Original Article

Assessment of the basaltic rocks in Yemen for the basalt fibers production

Amer M. Al-Sabri

Department of Geology and Environment, Faculty of Applied Science, Thamar University, Dhamar 87246, Yemen.

Corresponding author: Amer M. Al-Sabri, E-mail address: assabriamer2017@gmail.com

Received: 17 October 2024. Received (in revised form): 9 November 2024. Accepted: 12 November 2024. Published: 26 December 2024.

Abstract

Representative samples were collected from 22 sites across Yemen. The geochemical analysis found that the SiO_2 content ranges from 40.40 to 55.60%, the Al_2O_3 content ranges from 12.70 to 16.10%, the Fe_2O_3 content ranges from 8.41 to 15.80%, the CaO content ranges from 3.66 to 11.05%, and the MgO content ranges from 1.30 to 11.40%. TiO_2 content ranges from 1.11 to 5.56%, NaO_2 content from 1.88 to 4.88%, and K2O content from 0.67 to 3.25%. The calculations of the acidity, viscosity modules and fusibility constant of the investigated rocks showed the suitability of the basaltic rocks locations for the production of basalt fiber, except the Hajda, Mafraq Al Makha, Karish, Wadi Al Jima, and Wadi Qaradh locations, as a result of the high acidity module The results of the geochemical analysis of the studied samples were compared with the geochemical analyses of similar rocks from different countries used in basalt fiber production. The comparison showed significant similarities in the results, indicating that the studied rocks are suitable for basalt fiber production. A petrographically study on basalt rocks after they melted at temperatures ranging between 1190 and 1240 °C, and it was found that they consist mainly of basalt glass. Melting experiments were carried out, which showed that the beginning of the fusion was at a temperature ranging between 1030 and 1150 °C, and the fusion was completed at a temperature ranging between 1200 and 1220 °C, while the temperature at which the crystallization process began was at a temperature ranging between 1190 and 1200 °C. The study concluded that the studied basalt rock sites are suitable for manufacturing basalt fiber.

Keywords: Basalt; Fiber basal; Geochemical analysis; Yemen.

1. Introduction

Basalt is an extrusive igneous rock that forms from the rapid cooling of lava flows. It is characterized by its fine-grained texture and mafic mineral composition. Basaltic rocks are among the most common, forming lava plateaus and volcanic cones. Chemically, these rocks are considered very stable and inert [1, 2].

Basalt rocks are used in many constructions and industrial applications, the most important of which is the manufacture of basalt fibers [3]. Basalt is the raw material necessary to produce basalt fiber, which currently makes up one-third of the igneous rocks that make up the Earth's crust [4]. Basalt is environmentally friendly and non-hazardous and can be used for multiple industrial applications [5].

The lower the amount of remaining olivine in the basaltic melt, the higher the consistency of the melt, its fabric-forming ability, and its ability to form fibers [6, 7]. This offers the prospect of a completely new range of composite materials and products. Low-cost, high-performance fibers offer the potential to solve the largest problem in the cement and concrete industry: cracking and structural failure of concrete [8, 9].

2. General Geological Setting

Continental flood basalts (CFBs) form part of large igneous provinces (LIPs) that erupt onto continental crust. Continental plateau basalt covers large areas with thicknesses reaching thousands of meters. It is found in continental regions, forming plateaus such as the Deccan Plateau in India, the Columbia River Plateau in northwest America, the Parana Basin in southern America, the Karoo Basin in Africa, Australia, Siberia, Ethiopia, Yemen, Saudi Arabia and the Qatrani basalt in Egypt (Figure 1) [6, 10-12].

Basalt rocks are found in Yemen within the rocks of the Yemen Volcanic Group (YVG) in the form of plateaus within the Yemeni Trap Series (YTS) and volcanic cones within the Yemen Volcanic Series (YVS) [1, 12]. The basalt rocks found within the Yemeni Trap Series are distinguished by their compact structure and fine-grained texture and are widespread throughout the various governorates of Yemen (Figure 2). The total estimated reserves of basaltic rocks in Yemen are about 142 million cubic meters [3].

3. Materials and methods

Fieldwork involved collecting 22 representative samples of basaltic rocks from various governorates in Yemen (Figures 3 and 4). Petrographic analysis was conducted on 22 samples at the Yemeni Geological Survey laboratories using a Nikon optical polarizing microscope. The melting experiments were performed in the same laboratory's smelting furnaces. Geochemical analysis was carried out at the Saudi Geological Survey laboratories using X-ray fluorescence spectrometry (XRFS) on a fully automatic Philips PW2440 MagiX PRO wavelength-dispersive spectrometer equipped with a 66 kV generator and a 4 kW rhodium end-window X-ray tube.

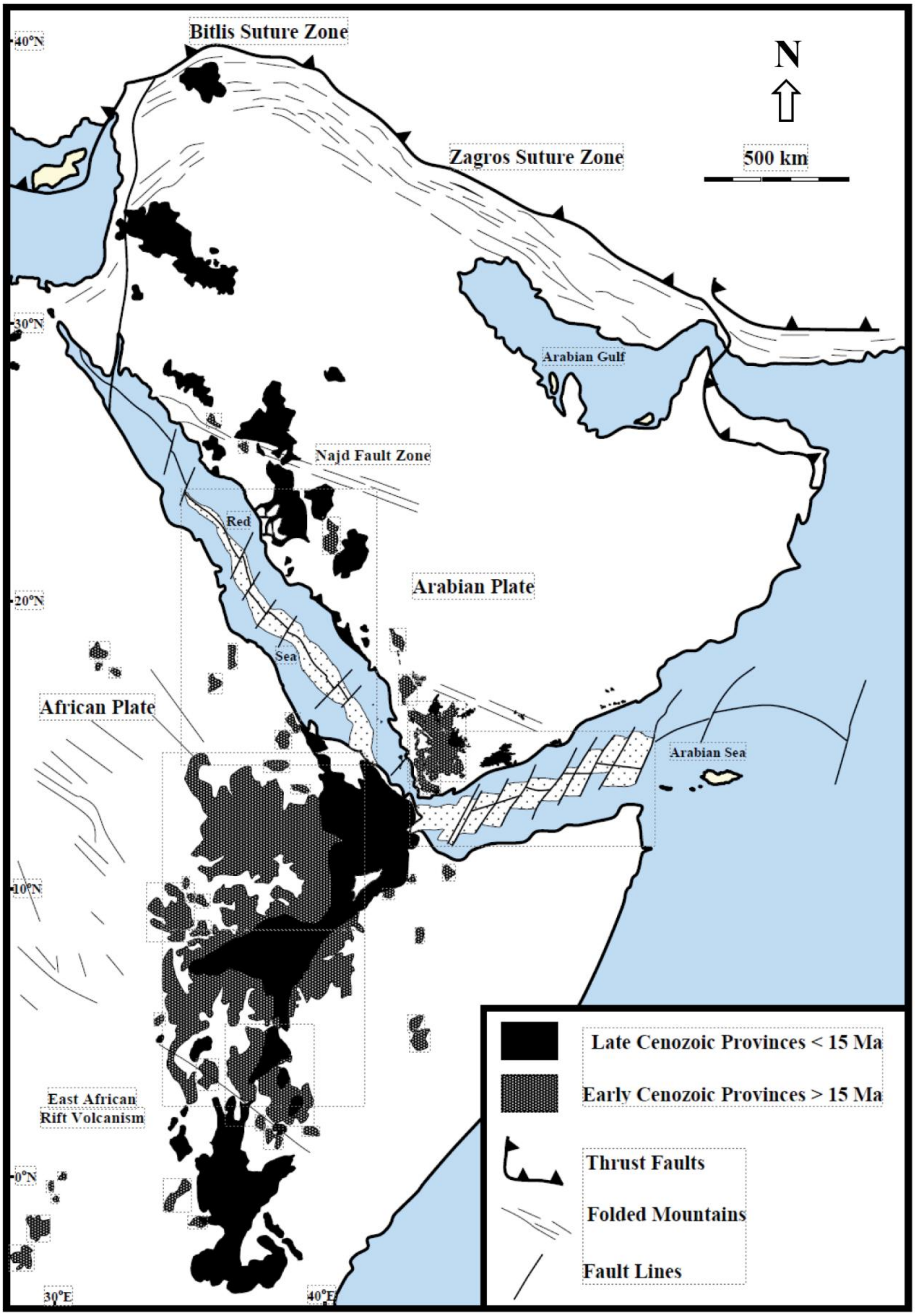

Figure 1: Simplified Geological map showing the distribution structure and Cenozoic volcanism around the Red Sea, Gulf of Aden, Afar, and adjacent areas [1]. Copyright 2009 Sana'a University.

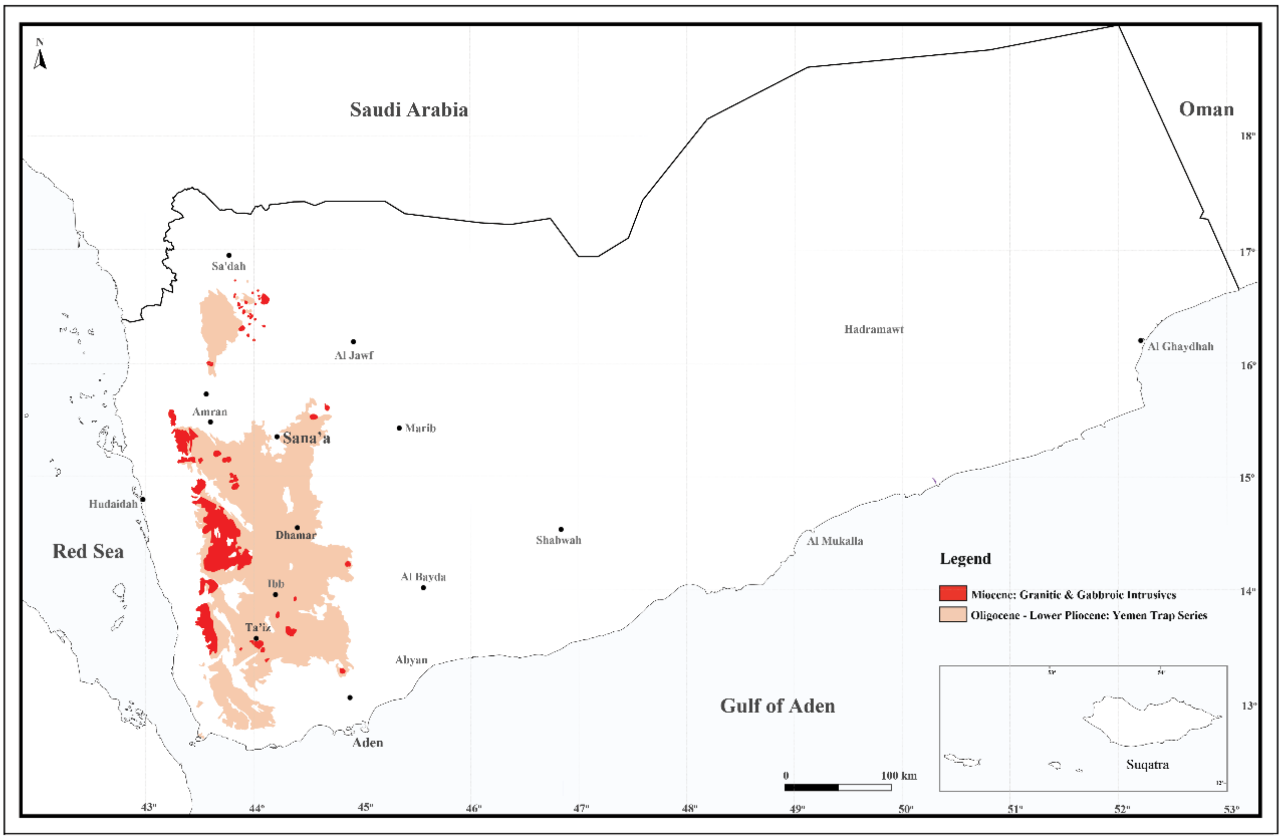

Figure 2: Geological map of Yemen Volcanic Series (Modified by Al-Sabri, 2020). Copyright 2020 Geological Survey & Mineral Resources, Sana'a, Yemen.

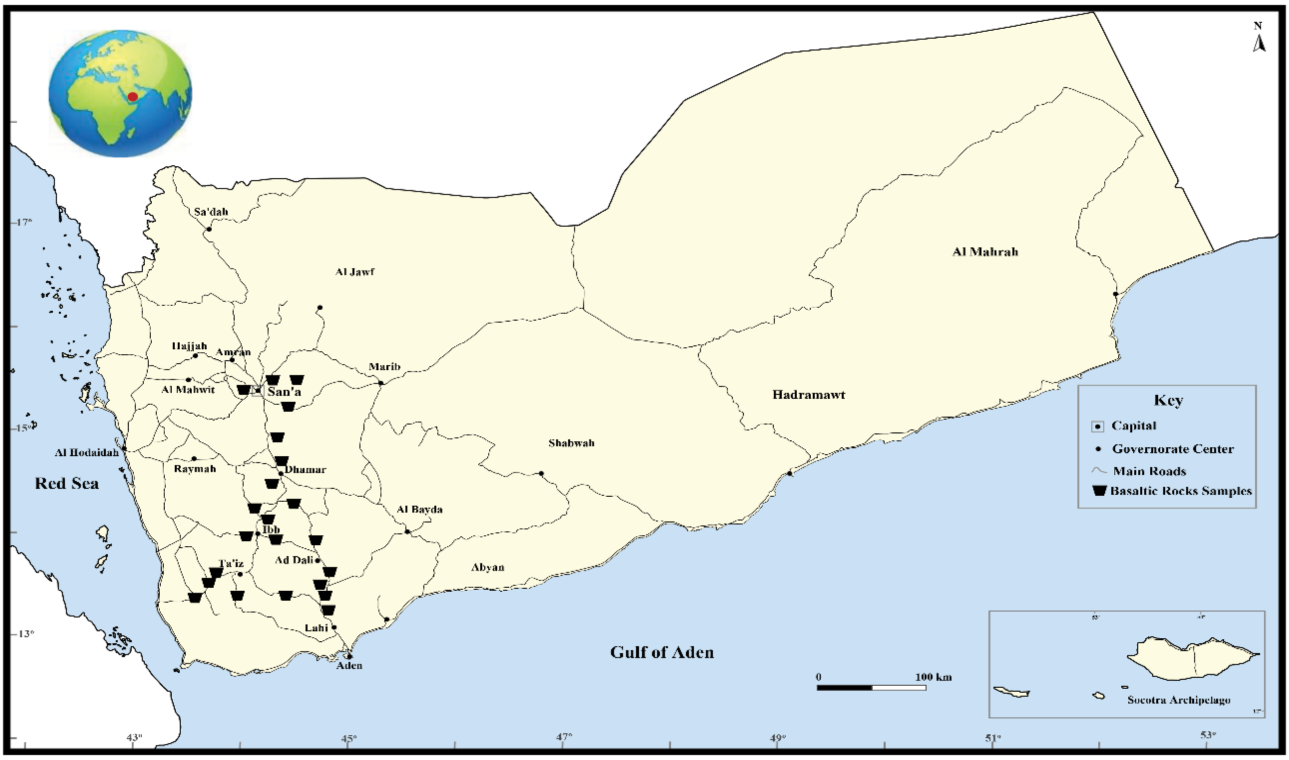

Figure 3: A location map of the study area showing the sites of collected samples.

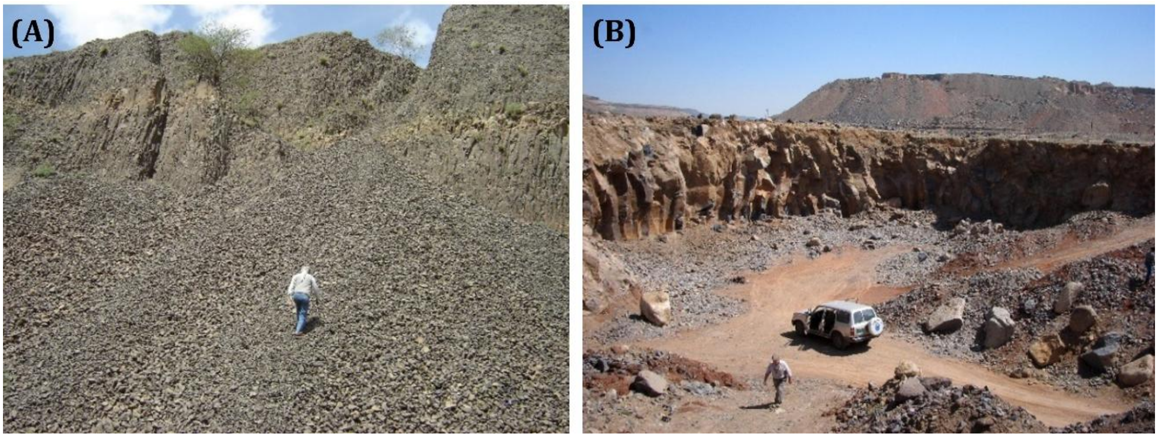

Figure 4: Outcrops of basaltic rocks (A) East of Ma'bar. (B) Al Subahah.

4. Results and Discussion

4.1 Results

4.1.1 Geochemistry

Geochemical analysis was carried out on twenty-two samples. The analysis included oxides of the major elements, SiO_2, Fe_2O_3, Al_2O_3, CaO, MgO, Na_2O, K_2O, and TiO. It was found that the SiO_2 content ranges from 40.40 to 55.60%, the Al_2O_3 content ranges from 12.70 to 16.10%, the Fe_2O_3 content ranges from 8.41 to 15.80%, the CaO content ranges from 3.66 to 11.05%, and the MgO content ranges from 1.30 to 11.40%. TiO_2 content ranges from 1.11 to 5.56%, NaO_2 content from 1.88 to 4.88%, and K_2O content from 0.67 to 3.25% (Table 1).

4.1.2 Petrographically study

Petrography was carried out on basalt rocks after they melted at temperatures ranging between 1190 and 1240 °C, and it was found that they consist mainly of glass, in addition to plagioclase and olivine (Figure 5A). The basalt rocks before the melting showed augite phenocrysts (Figure 5B).

The basaltic rock samples of the study area are dark and fine-grained. The main components of basaltic rocks are as follows:

Plagioclase: Plagioclase crystals are the predominant minerals in thin sections of all samples and occur in a lath-like, subhedral to euhedral tabular shape (Figure 6A).

Pyroxene: Pyroxene occurs as colorless to grayish brown in color with euhedral to subhedral pyroxene phenocryst crystals, forming ~22% of the rocks (Figure 6B).

Olivine: Olivine phenocrysts occur as single or clustered euhedral to anhedral crystals, forming ~12% of the rocks (Figure 5A).

Based on the petrographic study, it was found that the studied rocks are composed of basalt glass. Melting experiments were examined, which showed that the beginning of the fusion was at a temperature ranging between 1030 and 1150 °C, and the fusion was completed at a temperature ranging between 1200 and 1220 °C, while the temperature at which the crystallization process began was at a temperature ranging between 1190 and 1200 °C (Table 2), which are good indicators of the suitability of using basalt rocks in Yemen to form basalt. fibers for multiple construction and industrial applications.

Table 1: Geochemical composition of basaltic rocks in Yemen.

Localities	SiO_2	TiO_2	Al_2O_3	Fe_2O_3	MgO	CaO	Na_2O	K_2O
Jihanah	46.18	3.20	13.79	14.74	4.80	11.30	2.58	0.58
Bani Hushaish	44.50	5.56	13.40	15.53	4.89	10.40	2.22	0.84
W. Al Rawnah	46.85	4.14	12.80	15.97	4.75	8.94	3.90	1.25
Al Subahah	48.80	2.20	14.20	11.60	7.27	9.00	4.60	1.07
East of Ma'bar	44.03	3.86	15.80	7.41	8.97	10.50	2.20	1.12
Rusabah	47.80	3.75	13.90	11.60	4.12	7.70	4.53	1.40
A'med	48.10	2.67	14.60	12.82	6.23	9.60	3.24	0.83
Al Qawfa'ah	40.40	5.18	12.70	15.44	8.50	11.05	2.82	1.44
Al Dalil	49.15	4.29	13.40	13.72	4.56	8.60	2.77	1.12
Manwaz	48.00	2.49	15.40	11.20	7.68	9.70	3.17	1.02
Negd Al Juma'y	46.06	4.68	13.95	15.80	4.72	9.16	2.90	0.67
Al Udayn	50.30	4.07	14.30	11.98	4.26	8.75	2.42	1.05
Hajdah	52.00	3.20	14.88	11.01	3.59	6.22	3.46	1.85
Khuzaigah	45.50	3.22	15.00	13.31	6.41	10.60	2.56	0.90
Mafraq Al Makha	52.60	1.95	15.90	10.78	3.00	6.78	3.31	1.55
Al Nashamah	48.60	4.68	14.40	13.36	4.98	8.70	2.82	1.14
Karish	52.06	2.77	14.50	12.46	3.98	8.20	3.00	0.76
Al Anad	44.40	2.19	14.20	11.40	3.55	9.50	2.86	1.03
W. Al Jima	54.30	1.11	15.80	9.18	1.30	5.70	4.88	1.52
Al Ghayl	46.26	2.74	12.76	12.11	11.40	9.80	1.88	0.70
W .Qaradh	55.60	1.51	16.00	8.41	2.36	3.66	3.91	3.25
Al Erfaf	47.80	3.29	16.10	13.54	4.99	7.52	3.00	1.21

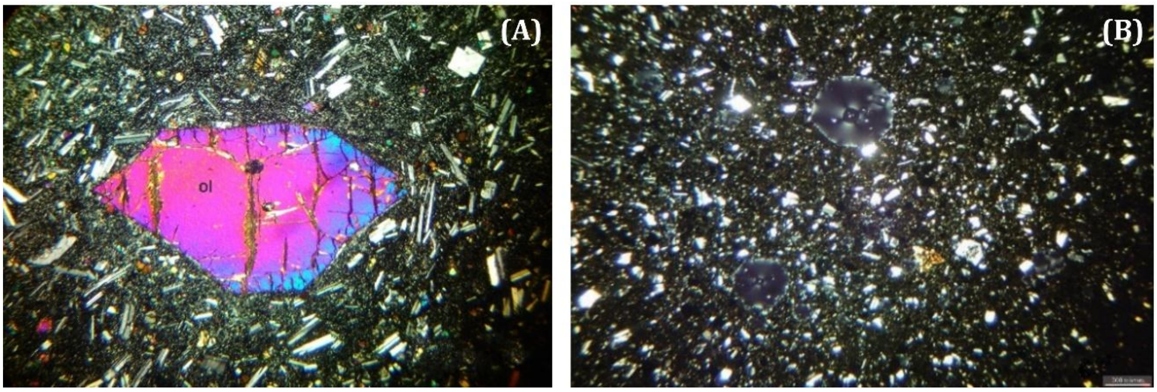

Figure 5: (A) Microphotographs of basalt rocks before the smelting showing the appearance of ol. phenocrysts. (B) Microphotographs of basalt rocks after the melting show the glassy structure.

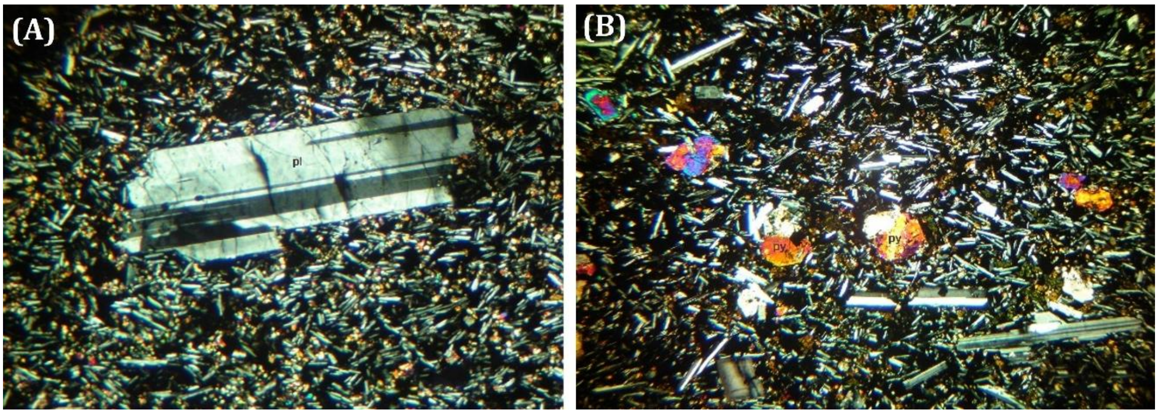

Figure 6: (A) Microphotographs of basalt rocks before the smelting showing the appearance of pla. phenocrysts. (B) Microphotographs of basalt rocks before the smelting showing the appearance of py. phenocrysts.

Table 2: Melting experiments results of basaltic rocks in Yemen.

Localities	Temperature (°C)		
	Initial Fusion	Total Fusion	Initial Crystallization
Jihanah	1165	1220	1200
Bani Hushaish	1150	1190	1180
W. Al Rawnah	1150	1195	1185
Al Subahah	1160	1200	1190
East of Ma'bar	1150	1190	1180
Rusabah	1165	1210	1195
A'med	1160	1195	1185
Al Qawfa'ah	1160	1195	1185
Al Dalil	1100	1190	1180
Manwaz	1155	1195	1185
Negd Al Juma'y	1155	1195	1185
Al Udayn	1140	1200	1190
Hajdah	1100	1200	1195
Khuzaigah	1150	1200	1190
Mafraq Al Makha	1100	1220	1200
Al Nashamah	1150	1200	1190
Karish	1050	1190	1180
Al Anad	1030	1200	1190
W. Al Jima	1030	1240	1220
Al Ghayl	1100	1220	1200
W .Qaradh	1030	1200	1190
Al Erfaf	1150	1220	1200

According to the Geochemical analysis result, the TAS diagram was plotted; it was found that most of the basalt rocks were in the area of the basalt type (Figure 7) [13, 14]. Based on the oxide values, a number of standards were calculated, which included the acidity module (Ma), which ranges between 2.72 and 11.89, the viscosity module (Mv), which ranges from 0.79 to 2.39, in addition to calculating the fusibility constant (R), which ranges from 3.10 to 6.19 (Table 3).

Table 3: Assessment Modules of basaltic rocks in Yemen.

Localities	Temperature (°C)		
	Viscosity Module (Mv)	Acidity Module (Ma)	Fusibility Constant (R)
Jihanah	1.8	3.72	4.05
Bani Hushaish	1.8	3.79	4.30
W. Al Rawnah	1.8	4.36	4.23
Al Subahah	1.6	3.87	3.50
East of Ma'bar	1.6	3.07	3.12
Rusabah	2.1	5.22	4.34
A'med	1.8	3.96	3.93
Al Qawfa'ah	1.2	2.72	3.10
Al Dalil	2.1	4.75	4.72
Manwaz	1.6	3.65	3.57
Negd Al Juma'y	1.8	4.32	4.61
Al Udayn	2.4	4.97	4.89
Hajdah	2.6	6.82	5.36
Khuzaigah	1.7	3.56	3.76
Mafraq Al Makha	2.9	7.00	5.55
Al Nashamah	2.0	4.61	4.59
Karish	2.4	5.46	5.13
Al Anad	2.3	4.49	4.26
W. Al Jima	3.8	10.01	6.00
Al Ghayl	1.2	2.78	3.11
W .Qaradh	3.6	11.89	6.19
Al Erfaf	2.0	5.11	4.83

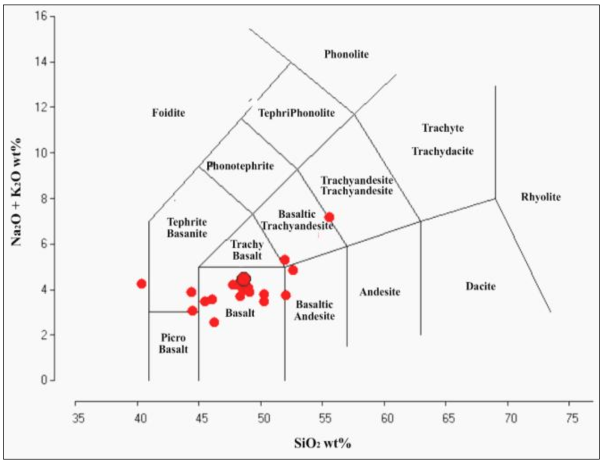

Figure 7: Total alkali-silica classification diagram [14]. Copyright 1992 Springer Nature.

The lower the remnant olivine in the basaltic melt, the higher the melt consistency and fabricability, and the better the fiber quality as well. The acidity modulus (Ma) for the raw basalt samples is calculated to evaluate the quality of the basaltic melt. The calculated acidity modulus (Ma) values would help predict the wool quality [6]. The acidity module (Ma), viscosity module (Mv), and fusibility constant (R) are calculated (Table 3) according to the following equations:

$$Ma = mSiO_2+mAl_2O_3 /mCaO+mMgO \quad (1)$$

$$Mv = xSiO_2+xAl_2O_3 /2xFe_2O_3+xFeO+xCaO+xMgO+xNa_2O \quad (2)$$

$$R=mSiO_2+mAl_2O_3+mTiO_2+mFe_2O_3+mFeO/mCaO+mMgO+mNa_2O+mK_2O \quad (3)$$

where m: mass content of oxides (wt.%) and x = molar content of oxides in mineral rocks (%).

4.2 Discussion

Geochemical analysis of basalt rocks in Yemen was compared with the Chemical composition of rocks for fiber production, which showed a similar composition with rocks for producing fibers (Table 4). The chemical composition of the rocks for producing fibers showed that the percentage of SiO_2 ranges from 39.0 to 55%, Al_2O_3 ranges from 10.0 to 20.0%, $FeO+Fe_2O_3$ ranges from 7.0 to 18.0%, MgO ranges from 3.0 to 12.0%, CaO ranges from 7.0 to 13.0%, K_2O+Na_2O ranges from 2.0 to 7.5%, TiO_2 ranges from 0.2 to 5.0%.

Geochemical analysis of basalt rocks in Yemen was compared with international analyses of basalt rocks from different countries, which are used to manufacture basalt fiber for all oxides that make up basalt rocks in Yemen (Table 5).

Based on oxide analysis, several standards were calculated. These include the acidity module (Ma), which ranges from 2.72 to 11.89; the viscosity module (Mv), which varies from 1.2 to 3.8; and the fusibility constant (R), which ranges from 3.10 to 6.19. The calculations of the acidity, viscosity modules, and fusibility constant of the basaltic rocks in Yemen showed the suitability of the basaltic rocks locations for the production of basalt fiber, except the Hajda, Mafraq Al Makha, Karish, Wadi Al Jima, and Wadi Qaradh locations, as a result of the high acidity module The high content of CaO and MgO in the andesitic basalt increases its crystallizing capacity and the smaller content of Al_2O_3 and a similar content of SiO_2 decrease the values of the acidic and viscosity modules. The basalt raw material's acidity modulus (Ma) is the main parameter defining the final fiber product quality [4, 15]. When the acidity modulus (Ma) value ranges between 2 and 2.7, the viscosity modulus (Mv) value ranges between 3.7 and 6, and the fusibility constant (R) value ranges between 2.3 and 4.4, the fiber is considered to be mineral wool [7].

The geochemical analysis of basalt rocks in Yemen was compared with the chemical composition of rocks used for fiber production (Table 5) and analyses of basalt rocks from different countries, which are used for the purpose of manufacturing basalt fiber [10]. The results showed similar compositions for all oxides that make up basalt rocks in Yemen.

The study concluded that the studied basalt rock sites are suitable for manufacturing basalt fiber, except the Hajda, Mafraq Al Makha, Wadi Al Jima, and Wadi Qaradh sites due to their high acidity standard.

Table 4. Chemical composition of rocks for fiber production [10].

Basic oxides	Content, wt. %	
	continuous fiber	staple fiber
SiO_2	47.0 - 55.0	39.0 - 51.0
Al_2O_3	14.0 - 20.0	10.0 - 19.0
$FeO+Fe_2O_3$	7.0 - 13.5	10.0 - 18.0
MgO	3.0 - 8.5	4.0 - 12.0
CaO	7.0 - 11.0	8.0 - 13.0
K_2O+Na_2O	2.5 - 7.5	2.0 - 5.0
TiO_2	0.2	2.0 - 5.0

Table 5. Chemical composition of basalts of different deposits [10].

Localities	SiO_2	Al_2O_3	Fe_2O_3	MgO	CaO	Na_2O+K_2O	TiO_2
Ukraine	49.03	12.58	14.03	5.47	9.53	3.00	2.85
	47.60	17.50	24.40	5.10	9.50	4.70	1.50
Georgia	50.61	16.75	10.26	4.65	9.07	4.88	1.81
Uzbekistan	48.54	14.40	11.65	7.18	9.88	3.99	2.14
	43.85	15.10	10.71	5.1	17.71	5.32	1.06
	47.05	15.74	8.71	5.44	8.45	4.99	-
	44.01	6.99	19.65	6.95	13.35	-	-
Kyrgyzstan	44.00	14.80	10.95	6.30	8.33	4.84	2.30
China	55.17	15.57	9.10	12.23	12.23	5.89	-
Russia	50.42	11.82	12.25	10.58	8.84	2.52	1.04
	49.92	15.96	9.39	8.22	10.52	2.85	0.68
	53.54	14.12	10.44	6.70	6.60	4.84	1.52
	51.70	17.00	12.90	5.29	7.00	3.81	2.20
	48.42	18.82	12.60	4.56	9.76	3.99	1.33
	48.70	15.90	20.80	5.40	12.90	3.50	0.80
	48.43	14.23	12.36	3.58	8.58	5.56	-
Indonesia	50.60	16.00	22.90	5.10	9.80	3.20	0.90
	48.60	16.70	11.69	4.47	6.25	7.40	2.12
Buryatia-Russia	44.28	15.21	13.92	8.58	9.61	5.24	2.08
	47.98	16.04	10.60	4.82	7.69	6.72	1.93

5. Conclusion

Based on the geochemical analysis of basalt rocks in Yemen and the oxide values, several standards were calculated, including the acidity module (Ma) and the viscosity module (Mv), in addition to calculating the fusibility constant (R). The study concluded that the studied basalt rock sites are suitable for manufacturing basalt fiber except the Hajda, Mafraq Al Makha, Wadi Al Jima, and Wadi Qaradh sites due to their high acidity standard.

Data Availability

The datasets used and analyzed during the current study are available from the corresponding author upon reasonable request.

Conflict of Interest

The authors declare no conflict of interest.

References

[1] Al-Sabri, A.M. (2009) Geology and Economic Potentiality of the Scoria Deposits in Dhamar – Rada' volcanic field, Yemen. *Earth and Environmental Sciences*, Ph.D. Thesis, Sana'a University, Sana'a, Yemen.

[2] Prakash, I., Pham, B.T. (2023) Geotechnical Evaluation of Basalt Rocks : a review in the context of the construction of Civil Engineering structures, *Journal of Science and Transport Technology* **3**: 10-24.

[3] Al-Sabri, A.M. (2020) Industrial Mineral in Yemen 2nd ed., Geological Survey & Mineral Resources, Sana'a, Yemen, pp. 85.

[4] Perevozchikova, B., Pisciotta, A., Osovetsky, B., Menshikov, E., Kazymov, K. (2014) Quality evaluation of the Kuluevskaya basalt outcrop for the production of mineral fiber, Southern Urals, Russia, *Energy Procedia* **59**: 309-314.

[5] Pérez, S.M. (202 (4Evaluation of Jordanian Basalt as a Thermal Insulation Material, *Journal of Ecological Engineering* **25**: 1–9.

[6] Farouk, M., Soltan, A., Farrag, A., El Kammar, A., Hamzawy, E. (2020) Utilization of some egyptian raw materials in rock wool industry: thermal and acoustic insulation, *Egyptian Journal of Geology* **64**: 155-165.

[7] Ksamentova, N., Kozhemjakina, N., Barantseva, S., Laktushin, A., Khvedchin, I., Mischenko, S. (2005) Prospects of using mafic rocks found in Southern Belarus for mineral fiber production, ed., UDC, pp. 476–513.

[8] Kumbhar, V.P. (2014) An overview: basalt rock fibers-new construction material, *Acta Engineering International* **2**: 11-18.

[9] Yan, L., Chu, F., Tuo, W., Zhao, X., Wang, Y., Zhang, P., Gao, Y. (2021) Review of research on basalt fibers and basalt fiber-reinforced composites in China (I): Physicochemical and mechanical properties, *Polymers and Polymer Composites* **29**: 1612-1624.

[10] Habib, M.K., Hafez, K.H., Shehata, W.M.(2001) *Saudi scoria & basalt: occurrences, uses and opportunities*; Jeddah, Saudi Arabi.

[11] Mattash, M.A. (1994) Study of the Cenozoic Volcanics and their associated intrusive rocks in Yemen in relation to rift development. *Geology*, Ph.D. Thesis, Hungarian Academy of Sciences, Budapest. Hungary.

[12] Al-Kadasi, M. (1994) The Temporal and Spatial Evaluation of the Basl Flow of the Yemen Volcanic Group. *Royal Holloway Collage*, Ph.D. Thesis, Landon University, London, United Kingdom.

[13] Ersoy, O., Aydar, E., Çubukçu, H.E. (2021) Geochemical evaluation of suitability of Central Anatolian (Turkey) volcanic rocks for rock fiber production, *Natural Resources Research* **30**: 1093-1104.

[14] Le Bas, M., Le Maitre, R., Woolley, A. (1992) The construction of the total alkali-silica chemical classification of volcanic rocks, *Mineralogy and petrology* **46**: 1-22.

[15] Ersoy, O., Aydar, E., Çubukçu, H.E., Atalay, C. (2022) Differentiation Index: A New Proxy for Determining Suitability of Volcanic Rocks for Production of Different Fiber Types, *Natural Resources Research* **31** : .130-117

TUJNAS

Thamar University Journal of Natural & Applied Sciences ***9***(2) (2024) 23–26

DOI: https://doi.org/10.59167/tujnas.v9i2.2313

Original Article

Concentration of total petroleum and total aromatic hydrocarbons in tar balls collected from the Red Sea coast of Yemen

Essam Nasher[1,*], Lee Yook Heng[2], Salmijah Surif[2], and Murad Ail Al-Salahi[1]

[1]Department of Marine Chemistry & Pollution, Faculty of Marine Sciences and Environment, Hodeidah University, Hodeidah, Yemen.
[2]School of Environmental and Natural Resources Science. Faculty of Science and Technology, Universiti Kebangsaan Malaysia (UKM), 43600 Bangi, Selangor, Malaysia.

*Corresponding author: E. Nasher at Department of Marine Chemistry & Pollution, Faculty of Marine Sciences and Environment, Hodeidah University, Hodeidah, Yemen, E-mail: nanasher2@gmail.com

Received: 10 November 2024. Received (in revised form): 6 December 2024. Accepted: 8 December 2024. Published: 26 December 2024

Abstract

The Red Sea is one of the main traffic routes of oil tankers, resulting in environmental damage and marine resource pollution due to the spillage. Quantitative analysis of tar ball was used to detect the concentrations of total petroleum hydrocarbons (TPHs) and total aromatic hydrocarbons (TAHs). In this study, six stations across the Red Sea coast of Yemen were selected according to their suitability and accessibility. An ultraviolet fluorescence technique was used to analyze the TPHs and TAHs after being extracted by an ultrasound-assisted solvent extraction procedure. The concentrations of TPHs ranged from 175.67 ± 11.20 mg/g to 708.55 ± 6.57 mg/g, and for TAHs were from 16.06 ± 1.89 mg/g to 48.25 ± 1.76 mg/g. The highest values of TPHs and TAHs were noticed in Ras Isa-II station, which reflected a continued oil spill from the Safir oil loading terminal. The study revealed significant environmental and health risks to marine organisms and humans.

Keywords: Tar ball; Petroleum Hydrocarbons; Aromatic Hydrocarbons; Red Sea; Yemen

1. Introduction

The rapid development of Yemen as an oil-producing country and its geographic position as one of the world's busiest shipping routes means a high risk of oil pollution in various forms. There are 25,000-30,000 ship transits annually in the Red Sea, and more than 100 million tons of oil are transported through the Red Sea annually [1]. There are no oilfields located along the coast of Yemen's Red Sea. Still, there are many petroleum service installations, such as the Safir terminal supertanker used for oil storage. Crude oil is supplied by pipeline from the Mariab oilfield to the Safir tanker and then transferred from it to other vessels, which causes oil spills or leakage during the loading process. A recent oil spill accident on the coast of Yemen occurred in October 2002 by a Lumburge oil tanker, spilling more than 17,000 tons of discharges to the Gulf of Aden [2]. Yemen, like many countries of the world, could be affected by oil pollution due to its position in the busiest shipping route.

Tar balls are stranded oil residues that include a complex mixture of hydrocarbons, aliphatic, aromatics, and heterocyclic compounds. Tar balls have been used as an indicator of the impact of oil pollution [3]. Tar balls are fragments or lumps of oil weathered to a semi-solid or solid consistency, sticky to the touch, and are difficult to remove from contaminated surfaces [4]. During oil spills, the components of crude oil, particularly the heavier refined products, float on the ocean surface. It will undergo several physical, biological, and chemical processes, reaching the shoreline as tar balls [5]. The tar balls can be found in several sizes, from a few millimeters to tens of centimeters, and are generally spherical in shape [4].

Tar balls on the beaches can originate from both land and/or sea. Land-based sources comprise atmospheric input, storm sewer runoff, refineries, and oil waste. Marine-based sources include offshore petroleum production, drilling, onshore bulk oil storage or production facilities, marine transportation discharges, which comprise vessels pumping bilges and tank cleaning, and pipelines. In addition, the natural seepage from the ocean/sea floor is considered a source of tar balls [6,7].

Petroleum hydrocarbons (PHs) in the marine environment originate from crude oils, their different refined derivatives, and from combustion products of crude oil and other fossil fuels. There is a broad range of substances, from harmless n-alkanes to toxic and partly carcinogenic aromatic and heterocyclic compounds, e.g., benzo(a)pyrene and benzo(a)anthracene [8]. Aromatic hydrocarbons (AHs) have been presented in the environment as complex mixtures. Sixteen polyaromatic hydrocarbon compounds (PAHs) have been identified by USEPA as serious pollutants due to their toxic, mutagenic, and carcinogenic characteristics [9]. AH compounds are unusually more stable and unsaturated; their stability permits them to be important constituents of oil pollution [10]. Moreover, aromatic hydrocarbons can be divided into two groups based on their properties and molecular weight: the low molecular weight AHs with two or three benzene rings and the high molecular weight AHs with four to six aromatic rings [10].

To the best of the researcher's knowledge, only a few studies on the total petroleum hydrocarbons and aliphatic fraction have been done on tar balls and sediments on the Red Sea coast of Yemen [6,11,12,13,14,15,16]. Abu Bakr [15] studied the distribution of n-alkanes in recent sediments on the Red Sea coast of Yemen from 1995 to 1997. The concentration of *n*-

alkanes in sediments from non-detectable to 1651 ng/g dry weight expressed as Kuwait crude oil equivalent. Al-Shwafi [16] identified the occurrence of oil and oil-products pollution along the Red Sea of Yemen. The concentration of aliphatic hydrocarbons ranged between 2.46 to 22.8 μg/g dry weights in sediment. In the tar ball samples from the same area, the Aliphatic concentrations were between 0.100 and 1.560 ug/g [6]. For the total Aromatic hydrocarbons (TAHs), there is no data available for tar balls from the Red Sea coast of Yemen. Moreover, the toxic effect of aromatic hydrocarbons to aquatic organisms are more serious than aliphatic. Therefore, the present study determined the concentrations of TPHs and TAHs in tar balls from the Red Sea Coast of Yemen to know the current state of oil pollution in this area of the Red Sea.

2. Materials and Method

2.1 Study Area

The sampling stations were between Khawidah and Alsallif (latitude 42°67.0 E 16°15.3 N and longitude 43° 23.0 E 13°55.0 N, Figure 1). These stations cover the coastal lines of Hodeidah city across the Red Sea of Yemen.

2.2 Samples collection

The tar ball samples were collected carefully by spoon and cleaned from debris like sand or coral using a brush. They were then wrapped in aluminum foil and then kept in plastic bags (Ziploc) and stored in a dark place for transport to the laboratory. The tar ball samples were stored under -5 ºC until analyzed.

2.3 Chemical analysis

Extraction of extractable organic matter (EOM) and analysis of total petroleum hydrocarbons (TPHs) and total aromatic hydrocarbons (TAHs) were performed following the procedure described by Hegazi [17]. The tar ball (100 mg) was mixed with approximately 250 mg of anhydrous sodium sulfate Na_2SO_4 (activated at 400ºC for 2 hours) and then extracted with 20 ml of *n*-hexane/dichloromethane (DCM) (1:1 v:v) for 15 mins using the ultrasound-assisted solvent extraction technique (sonication bath) to obtain the liquid layer. The extraction was repeated twice. The combined extracts were filtered by a Glass Fiber Filter (GF/F) of 0.45µm to remove any particulates from the solution. The extracts were concentrated to approximately 5 ml using rotary evaporation. The EOM was transferred to 10 ml of a pre-weighed vial and then dried under nitrogen steam. The constant weight of the vial to obtain the EOM was recorded. The EOM was redissolved in a 25 ml volumetric flask with an n-hexane solvent. The sample extracts, which include the TPHs and TAHs, were measured using an ultraviolet fluorescence technique (UVF, Perkin Elmer model LS 55-Luminescence spectrometer) at excitation and emission wavelengths of 310 and 360 nm, respectively. The Marib light crude oil was used as the equivalent standard in Yemen for measuring TPHs [6]. The chrysene standard was used as equivalent standard for measuring TAHs in tar balls.

2.4 Quality control and data analysis

Quality control and quality assurance were applied to all data. Replicate samples were analyzed for each station to calculate the precision of measurements. Procedural blanks were used between each batch of two samples to prevent contamination and detect interference. The density measurement of samples was minimized from the interference density detected in the blank. Detection limits of the ultraviolet fluorescence technique were between 1 ppm and 5 ppm, according to the Naval Facilities Engineering Command [18]. Thus, the extracts were diluted to give a reading within detection limits and the linear calibration range of the fluorimeter. Marib light crude oil equivalent and Chrysene standard calibration standards were run at the beginning of each working day before analyzing samples to estimate the regression equations used to calculate the concentration of TPHs and TAHs in the tar balls, respectively. Linear relationships were obtained with correlation coefficients (r) from the linear regression of $r = 0.99$ for Marib light crude oil equivalent and $r = 0.9914$ for Chrysene. Regression equations obtained an r value of ≥ 0.99 are acceptable according to the Environmental Protection Agency.

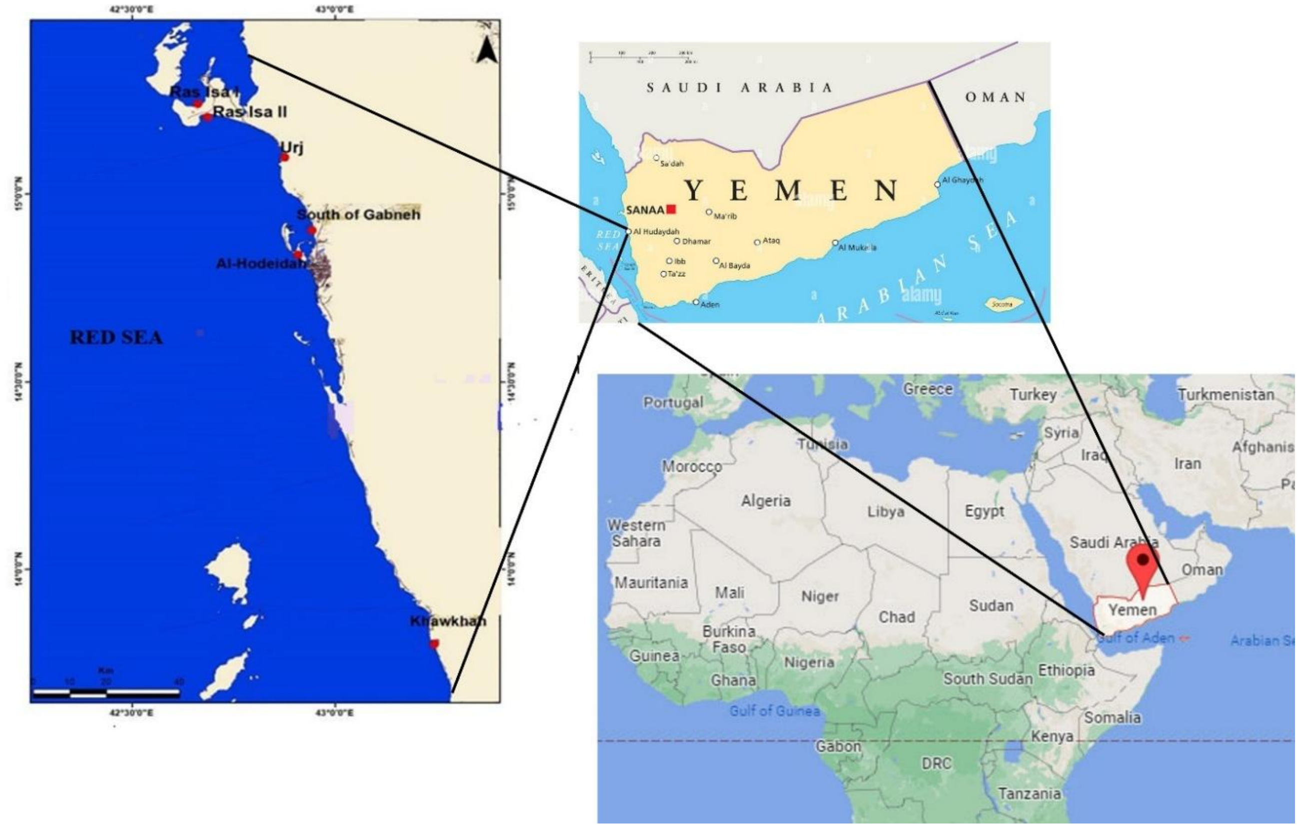

Figure 1: Sampling stations in the Red Sea coast of Al-Hodeidah, Yemen.

3. Results and Discussion

3.1 Total Petroleum Hydrocarbons (TPHs) in Tar Balls

Figure 2 shows the concentrations of TPHs by Marib light crude oil equivalent in the tar ball samples. The concentrations of TPHs vary to a wide range: from 175.67 ±11.20 mg/g at Ras Isa I station to 708.55 ±6.57 mg/g at Ras Isa II station, the mean concentration of which was 444.75 ±17.42 mg/g. The high concentration was found at Ras Isa-II station, which was expected due to the continuous deposition of petroleum hydrocarbons derived from different sources. For example, the oil spill that occurred during the load and transport of crude oil from the Safir oil loading terminal or from an adjacent area to a fuel storage depot at the coastal line is one of the important sources of oil pollution in this area. The same station, Al-Salif or Ras Isa –II, showed a high concentration of aliphatic in the tar ball found by Alshawfi [6]. The same input source was concluded: the Ras Isa oil loading terminal, which affected the area. Moreover, under favorable wind and currents, a portion of the oil leakage was deposited along the coastal stretch around Ras Isa II station. Furthermore, from the field observations, the gentle slope of the shoreline can increase the accumulation of tar balls on it. The slope of the shoreline was so high that it may have saved the tar balls from the weathering factors. The concentrations of TPHs in other stations, Urj, South of Gabaneh, Hodeidah, and Khawkhah samples were 487.69 ± 34.39, 364.45 ± 5.52, 463.41 ± 16.79 and 468.72 ± 30.02 respectively. Variations of concentration in these stations were slight and may be due to their similar sources of petroleum hydrocarbons or similar activities, which include fishing boats, changing engine oil, and discharging dirty ballast water from tankers before reaching the oil loading terminal. In contrast, the low concentration was 175.67 ±11.20 mg/g at Ras Isa -I station, which could indicate the low oil spill or may be due to low activities in the Alsalaf port. Petroleum hydrocarbons in the tar balls and sediments of Yemen and other regions of the Red Sea pose significant environmental and health risks. Research shows that these petroleum hydrocarbons can severely impact marine life, leading to bioaccumulation in the food chain and causing physiological and reproductive issues in aquatic organisms [19]. The socio-economic impacts of petroleum hydrocarbons in the tar balls include loss of fish and crustaceans, eutrophication of water bodies, abandonment of fishing grounds and associated livelihood pursuits, degradation of aquatic resources, and ecological damage [20]. The tourism sector is affected by tar ball pollution, which causes tourists to migrate from the beach and causes economic losses.

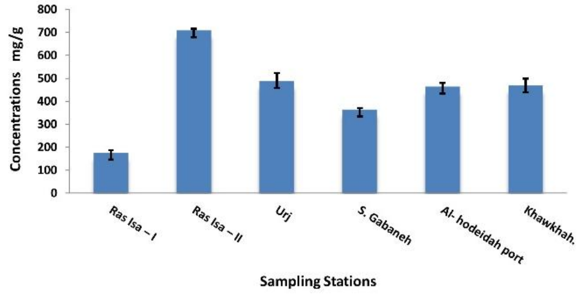

Figure 2: Concentrations of Total Petroleum Hydrocarbons (TPHs) in the tar balls.

3.2 Total Aromatic Hydrocarbons (TAHs) in Tar Balls

Chrysene standard was used widely to reveal the total aromatic hydrocarbons (TAHs) in the sample extracts by an ultraviolet fluorescence technique [21]. Figure 3 shows the concentrations of TAHs in the tar ball samples. The concentration range of TAHs was between 16.06 ± 1.89 mg/g at South of Gabaneh station to 48.25 ± 1.76 mg/g at Ras Isa II station, and the mean concentration was 28.98 ±1.36 mg/g. The same station, Ras Isa-II, recorded high concentrations of TAHs and TPHs, which represented the same source of oil pollution. Clearly, the continuous deposition of petroleum hydrocarbons derived from the oil spill that occurred during the load and transport of the crude oil from the Safir oil loading terminal or from an adjacent area to a fuel storage depot at the coastal line was considered the main sources of TAHs and TPHs. In the second station for the same location that Ras Isa labeled, I recorded a concentration of 39.50 ± 0.70 mg/g, close to that of Ras Isa II station. Both of these stations reflected the same sources of oil pollution. The concentrations of TAHs in Urj, Hodeidah, and Khawkhah samples were 25.13 ±1.55, 19.73 ±0.39, and 25.28 ±1.82 mg/g, respectively. The concentrations in these stations were slightly different, which may indicate the similarity of the oil pollution sources or/and their effect by the same level of weathering factors. The possible sources of TAHs in these stations could result from continuous deposition of PAH derived from heavy, light crude oil spills and/or used crankcase oil of fish boats and water balance from tankers. Similar possible sources have been found worldwide in many tar ball samples [22, 23, 17]. The same sources were suggested by DouAbul [24] when high concentrations of polyaromatic hydrocarbons were found in fish of the Red Sea. The impact of aromatic hydrocarbons on aquatic environment lei on their toxicity. The other types of toxicities that TAHs cause on aquatic organisms and from them to human society are developmental toxicity, genotoxicity, immunotoxicity, oxidative stress, and endocrine disruption, and the most concerning toxicity is their carcinogenicity [25].

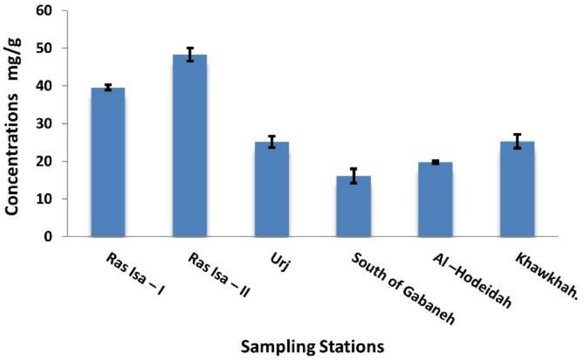

Figure 3: Concentrations of Total Aromatic Hydrocarbons (TAHs) in the tar balls.

3.3 Extractable organic matter (EOM) in tar ball

Figure 4 shows no strong correlation between the EOM of the tar balls and the concentration of TPHs. Indeed, the hydrocarbons in the samples were not related to the concentration of EOM (R^2= 0.21). Likewise, the relationship was positive, but the correlation was not strong between the EOM and TPHs, suggesting that the organic matter does not govern the observed distribution of petroleum hydrocarbons associated with tar balls; therefore, they may be controlled by various sources of inputs and/or differing transport processes [26,27].

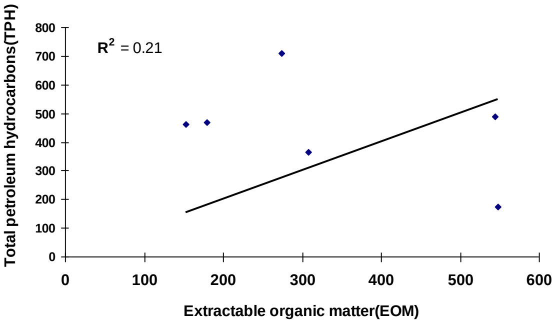

Figure 4: Correlation of total petroleum hydrocarbons against extractable organic matter for tar balls.

Figure 5 shows the concentrations of EOM in tar ball samples. The concentrations of EOM ranged from 153.00 ±9.00 to 548.00 ±54.00 mg/g, with the mean concentration 334.42 ±31.08 mg/g. The significant concentrations were found in Ras Isa I (548.00 ±54.00 mg/g) and Urj (544.50 ±75.50 mg/g). These high results could be affected by both natural (plants, animals, and microorganisms) and anthropogenic input (oil spill, sewage, agricultural drainage). Notably, the lowest value was observed in Al-Hodeidah station (153.00 ± 9.00 mg/g). The reasons for the high or low concentrations of EOM in the several stations were probably caused by sea grass, algae, mangroves, and plankton as natural sources or may be due to untreated sewage, port activities, and/or adjacent fuel storage depot at the coastal area. Other reasons can be due to the contaminated sediments and water, which are likely to enter the sea as well as be deposited in the shoreline through valley run-offs during seasonal rainfall [2].

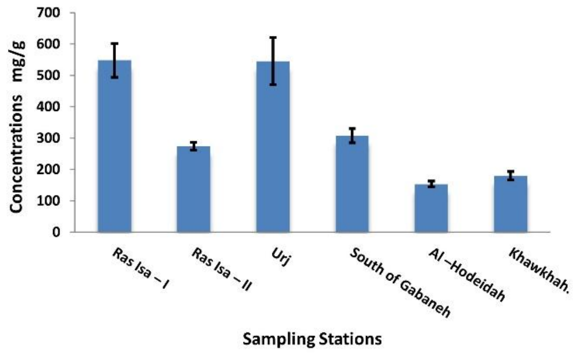

Figure 5: Concentrations of extractable organic matter (EOM) in the tar balls.

4. Conclusion

The concentrations of hydrocarbon partitions, total petroleum hydrocarbons (TPHs), and total aromatic hydrocarbons (TAHs) were measured in tar balls collected from the Red Sea coast of Al-Hodeidah, Yemen. The high concentrations of TPHs and TAHs in some sampling stations were due to the continued deposition of crude oil that occurred during the load and transport of the crude oil from the Safir oil loading terminal and oil spill from other tankers. The concentrations of TPHs and TAHs can pose significant environmental and health risks to marine organisms and humans. Annual monitoring of oil pollution on the coast of the Red Sea by using water, sediments, tar balls, and local fish is encouraged to protect and sustain the Red Sea resources.

Data Availability

The datasets used and analyzed during the current study are available from the corresponding author upon reasonable request.

Conflict of Interest

The authors declare no conflict of interest.

References

[1] Gladstone, W., Tawfiq, N., Nasr, D., Andersen, I., Cheung, C., Drammeh, H., Krupp, F., Lintner, S. (1999) Sustainable use of renewable resources and conservation in the Red Sea and Gulf of Aden: issues, needs and strategic actions, *Ocean & Coastal Management* **42**: 671-697.

[2] The Protection of the Marine Environment From Land-Based Activities (NPA).(2003) *Yemen's National Programme of Action for the Protection of the Marine Environment from Land-Based Activities*; Minister of Water and Environment, Sana'a, Yemen.

[3] Clark, R.B. (2002) Marine pollution, 3rd ed., Oxford University Press, UK, pp. 220.

[4] Goodman, R. (2003) Tar Balls: The End State, *Spill Science & Technology Bulletin* **8**: 117-121.

[5] Chandru, K., Zakaria, M.P., Anita, S., Shahbazi, A., Sakari, M., Bahry, P.S., Mohamed, C.A.R. (2008) Characterization of alkanes, hopanes, and polycyclic aromatic hydrocarbons (PAHs) in tar-balls collected from the East Coast of Peninsular Malaysia, *Marine Pollution Bulletin* **56**: 950-962.

[6] Al-Shwafi, N.A. (2000) Beach Tar along the Red Sea Coast of Yemen—Quantitative Estimation and Qualitative Determination ". *Earth and Environmental Sciences*, Ph.D. Thesis, Sana 'a University.

[7] Gabche, C.E., Folack, J., Yongbi, G.C. (1998) Tar ball levels on some beaches in Cameroon, *Marine Pollution Bulletin* **36**: 535-539.

[8] Bleeker, E.A.J., Pieters, B.J., Wiegman, S., Kraak, M.H.S. (2002) Comparative (Photoenhanced) Toxicity of Homocyclic and Heterocyclic PACs, *Polycyclic Aromatic Compounds* **22**: 601-610.

[9] Nasher, E., Heng, L.Y., Zakaria, Z., Surif, S. (2013) Assessing the Ecological Risk of Polycyclic Aromatic Hydrocarbons in Sediments at Langkawi Island, Malaysia, *The Scientific World Journal* **2013**: 858309.

[10] Tam, N.F.Y., Ke, L., Wang, X.H., Wong, Y.S. (2001) Contamination of polycyclic aromatic hydrocarbons in surface sediments of mangrove swamps, *Environmental Pollution* **114**: 255-263.

[11] Douabul, A.A., Al-Shwafi, N.A.(1996) Composition and sources of hydrocarbons in the Red Sea and Gulf of Aden. 1st Conference on the Chemistry and Environment, Yemen Chemical Society, Sana'a, Yemen, pp. 20-24.

[12] DouAbul, A., Heba, H.(1996) *Investigation following a fish kill in Bab el-Mandeb Red Sea during November 1995*; Environmental Protection Council (EPC) (Dutch Support Project to Technical Secretariat EPC, Yemen), Yemen,

[13] Al-Shwafi, N.A. (1997) A Baseline Study on Petroleum Hydrocarbons in Southern Red Sea. *Earth and Environmental Sciences*, M.Sc. Thesis, Sana'a University, Sana'a. Yemen.

[14] Regional Organization for the Conservation of the Environment of the Red Sea and Gulf of Aden (PERSGA) (2001) Strategic Action Programme for the Red Sea and Gulf of Aden, Country Reports *The International Bank*, Washington, D.C., U.S.A.

[15] Al-Shwafi, N.A., Heba, H.M.A., DouAbul, A.A.Z. (2002) *N*-alkanes Distributions in surface sediments from the Red Sea coast of Yemen, *Faculty of Science Bulletin-Sana'a University* **15**: 59-65.

[16] Al-Shwafi, N.A. (2003) Distribution of aliphatic and polynuclear aromatic hydrocarbons (PAHs) in surficial sediments from the Red Sea of Yemen, *Journal of King Abdulaziz University: Marine Sciences* **14**: 89-97.

[17] Hegazi, A.H., Andersson, J.T., Abu-Elgheit, M.A., El-Gayar, M.S. (2004) Source diagnostic and weathering indicators of tar balls utilizing acyclic, polycyclic and S-heterocyclic components, *Chemosphere* **55**: 1053-1065.

[18] NAVFAC (Naval Facilities Engineering Command), *TechData Sheet,* (2000) Near-Real Time UV Fluorescence Technique for Characterization of PAHs in Marine Sediment. *NFESC TDS-2075-ENV, NAVFAC.* Washington, DC, USA, 10 June 2000. https://frtr.gov/pdf/uvfluorescence_2.pdf

[19] Neff, J.M. (2002) Bioaccumulation in marine organisms: effect of contaminants from oil well produced water, ed., Elsevier, Amsterdam, The Netherlands, pp. 468.

[20] Ipingbemi, O. (2009) Socio-economic implications and environmental effects of oil spillage in some communities in the Niger delta, *Journal of Integrative Environmental Sciences* **6**: 7-23.

[21] Tolosa, I., de Mora, S.J., Fowler, S.W., Villeneuve, J.-P., Bartocci, J., Cattini, C. (2005) Aliphatic and aromatic hydrocarbons in marine biota and coastal sediments from the Gulf and the Gulf of Oman, *Marine Pollution Bulletin* **50**: 1619-1633.

[22] Barakat, A.O., Mostafa, A.R., RullkÖtter, J., Rahman Hegazi, A. (1999) Application of a Multimolecular Marker Approach to Fingerprint Petroleum Pollution in the Marine Environment, *Marine Pollution Bulletin* **38**: 535-544.

[23] Pauzi Zakaria, M., Okuda, T., Takada, H. (2001) Polycyclic Aromatic Hydrocarbon (PAHs) and Hopanes in Stranded Tar-balls on the Coasts of Peninsular Malaysia: Applications of Biomarkers for Identifying Sources of Oil Pollution, *Marine Pollution Bulletin* **42**: 1357-1366.

[24] DouAbul, A.A.Z., Heba, H.M.A., Fareed, K.H.(1997) Polynuclear Aromatic Hydrocarbons (PAHs) in fish from the Red Sea Coast of Yemen. Asia-Pacific Conference on Science and Management of Coastal Environment, **123**: *Springer Netherlands*, Dordrecht, pp. 251-262.

[25] Honda, M., Suzuki, N. (2020) Toxicities of Polycyclic Aromatic Hydrocarbons for Aquatic Animals, *International Journal of Environmental Research and Public Health* **17**: 1363.

[26] Readman, J.W., Fillmann, G., Tolosa, I., Bartocci, J., Villeneuve, J.P., Catinni, C., Mee, L.D. (2002) Petroleum and PAH contamination of the Black Sea, *Marine Pollution Bulletin* **44**: 48-62.

[27] Turki, A. (2006) Hydrocarbon contamination in sediments from Obhur Creek, Jeddah, Saudi Arabia, *Bulletin of Pure & Applied Sciences-Geology* **25**: 41-41.

Thamar University Journal of
Natural & Applied Sciences

ISSN-Print: 203-0764
ISSN-Online: 2959-4340

TUJNAS

Volume 9, Issue 2, 2024

CONTENTS

Articles